NEUROSCIENCE

Reducing microglial lipid load enhances β amyloid phagocytosis in an Alzheimer's disease mouse model

Xiaoting Wu[1], James Alastair Miller[2], Bernett Teck Kwong Lee[2], Yulan Wang[2], Christiane Ruedl[1]*

Macrophages accumulate lipid droplets (LDs) under stress and inflammatory conditions. Despite the presence of LD-loaded macrophages in many tissues, including the brain, their contribution to neurodegenerative disorders remains elusive. This study investigated the role of lipid metabolism in Alzheimer's disease (AD) by assessing the contribution of LD-loaded brain macrophages, including microglia and border-associated macrophages (BAMs), in an AD mouse model. Particularly, BAMs and activated CD11c$^+$ microglia localized near β amyloid (Aβ) plaques exhibited a pronounced lipid-associated gene signature and a high LD load. Having observed that elevated intracellular LD content correlated inversely with microglial phagocytic activities, we subsequently inhibited LD formation specifically in CX3CR1$^+$ brain macrophages using an inducible APP-KI/*Fit2*$^{i\Delta M\varphi}$ transgenic mouse model. We demonstrated that reducing LD content in microglia and CX3CR1$^+$ BAMs remarkably improved their phagocytic ability. Furthermore, lowering microglial LDs consistently enhanced their efferocytosis capacities and notably reduced Aβ deposition in the brain parenchyma. Therefore, mitigating LD accumulation in brain macrophages provides perspectives for AD treatment.

INTRODUCTION

Lipid droplets (LDs) are highly dynamic, lipid-rich organelles, which are present in all cell types (*1*). Having long been viewed as inert, simple cytoplasmic storage sites for excess lipids, LDs are now recognized as specialized organelles, which fundamentally affect energy and lipid homeostasis (*1*). White adipose tissue constitutes the largest energy reservoir in the human body. This energy is stored in adipocyte LDs in the form of triacylglycerols, which are rapidly released as free fatty acids in times of energy demand (*2*). LDs are also present in immune cells, in particular macrophages, where they supply energy for the formation and maturation of phagosomes (*3*). LD accumulation in macrophages is associated with several inflammatory conditions (e.g., atherosclerosis) (*4*, *5*), infectious diseases (e.g., mycobacterial infections) (*6*, *7*), and cancer (*8*, *9*). LDs can also be found in macrophages residing in lipid-rich environments such as adipose tissue (*10*) and the brain (*11*). A subpopulation of adipose tissue macrophages expresses specific receptors and enzymes that permit efficient lipid uptake and buffering; these features enable the macrophages to progressively form LDs that aid lipid accumulation during adiposity (*10*). These lipid-associated macrophages potentially play an essential function in controlling tissue-level lipid homeostasis (*12*). Lipid-droplet accumulating microglia (LDAM) have been identified in aged brains of mice and classified as dysfunctional cells as they exhibit defective phagocytic activity and show increased production of pro-inflammatory cytokines and reactive oxygen species (ROS) (*11*) where they contribute to an impaired response of stroke (*13*). A recent study has defined the distinct stages of murine microglial activation in neurodegenerative diseases such as Alzheimer's disease (AD). The microglia expressed diverse genes associated with lipid homeostasis and LD accumulation, including apolipoprotein E (*Apoe*), lipoprotein lipase (*Lpl*), and triggering receptor expressed on myeloid cells 2 (*Trem2*) (*14*). One of the hallmarks of AD is the accumulation of β amyloid (Aβ) plaques in the brain. Microglia form a protective barrier around these Aβ plaques to safeguard the brain from their neurotoxic effects (*15*, *16*). However, perturbations in microglial activity, often associated with aging, can affect the effective clearance of these neuron-derived Aβ fibrils, leading to increased plaque formation and the progression of cognitive and behavioral impairments (*17*–*20*). The gradual appearance of a highly metabolically active subpopulation of CD11c$^+$ microglia around the plaques correlates with AD progression (*14*). While this observation represents progress in understanding the contribution of macrophages to AD pathogenesis, little is known about whether lipid metabolism affects the function of these macrophages and whether these cells have a role in neurodegenerative disorders. Therefore, the present study aimed to investigate the formation of LD-loaded brain macrophages during AD progression, focusing specifically on microglia and including distinct border-associated macrophages (BAMs), recently recognized for their potential contribution to central nervous system diseases (*21*–*23*). Furthermore, we studied the ability of LD-loaded microglia to clear Aβ and apoptotic neurons and explore strategies to enhance macrophagic phagocytic efficiency. For this purpose, we developed an APP-KI/*Fit2*$^{i\Delta M\varphi}$ transgenic mouse model that disrupts LD accumulation in CX3CR1$^+$ brain macrophages by targeting a fat storage–inducing transmembrane protein (FIT2), a key protein in LD biogenesis that facilitates LD formation from the endoplasmic reticulum (*1*). This mouse model allowed us to investigate the impact of reduced microglial LD content on their phagocytic activity and function in AD.

RESULTS

AD accelerates LD accumulation in brain macrophages

To investigate the lipid-storing capability of different brain macrophage subsets and gain more insights into the conditions triggering LD accumulation, we isolated bulk microglia and CD206$^+$ BAMs from 2- and 6-month-old healthy wild-type (WT) and *APP*$^{NL\text{-}G\text{-}F}$ (APP-KI) mice that were fed a normal regular chow diet (ND) or a high-fat diet (HFD) and stained them with the LD-specific dye BODIPY (Fig. 1A and fig. S1). Calculating the percentage of LD$^+$

---

[1] School of Biological Sciences, Nanyang Technological University, Singapore, Singapore. [2] Lee Kong Chian School of Medicine, Nanyang Technological University, Singapore, Singapore.
*Corresponding author. Email: ruedl@ntu.edu.sg

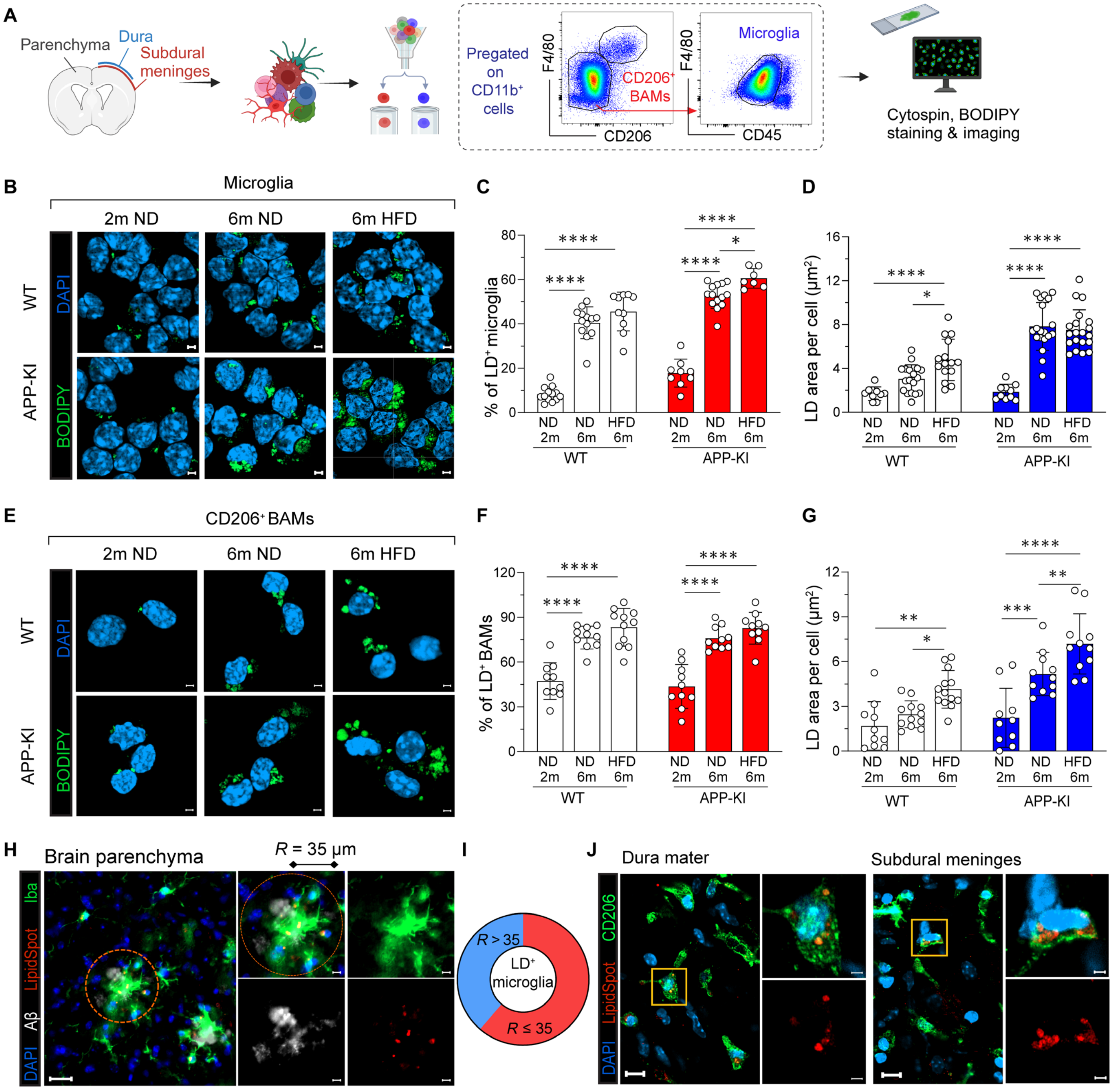

Fig. 1. AD accelerates LD accumulation in brain macrophages. (**A**) Schematic diagram showing the experimental design (image created with BioRender.com). (**B**) Representative confocal images showing DAPI (blue) and BODIPY (green) staining of sorted microglia from 2-month-old (2m) WT and APP-KI mice fed ND, 6-month-old (6m) WT and APP-KI mice fed ND, and 6-month-old WT and APP-KI mice fed HFD. Scale bars, 5 μm. (**C** and **D**) Bar chart (with individual values shown as dots) of the percentage of LD$^+$ microglia and the LD area per microglia. Each dot represents the average result calculated from one slide; three to five slides were evaluated per mouse and $n = 5$ mice per group. (**E**) Representative confocal images showing DAPI (blue) and BODIPY (green) staining of sorted BAMs. Scale bars, 5 μm. (**F** and **G**) Bar chart (with individual values shown as dots) of the percentage of LD$^+$ macrophage and LD area per macrophage. Each dot represents the average result calculated from one slide; three to five slides were evaluated per two to three pooled mice and $n = 6$ mice per group. (**H**) Representative images showing anti-Iba antibody (green), anti-Aβ antibody (white), LipidSpot 610 (red), and DAPI (blue) staining of the brain tissue from a 6-month-old HFD-fed APP-KI mouse. An area with a radius of <35 μm from the center of the plaque was defined as the plaque-proximal area. Scale bars, 20 and 5 μm (zoom-in). (**I**) Quantification of LD$^+$ microglia inside and outside the plaque-proximal area. (**J**) Representative confocal images showing CD206 (green), LipidSpot 610 (red), and DAPI (blue) staining of the brain border structures (dura mater and subdural meninges) from a 6-month-old HFD-fed APP-KI mouse. Scale bars, 10 and 2 μm (zoom-in). Samples were analyzed by two-way ANOVA. $*P < 0.05$; $**P < 0.01$; $***P < 0.001$; $****P < 0.0001$. For clarity, nonsignificant values are not shown.

microglia and the LD area within each cell revealed an age-related increase in LD accumulation (Fig. 1B). Specifically, the proportion of LD$^+$ microglia significantly increased from 5% (at 2 months) to 35% (at 6 months) in WT mice and from about 10% (2 months) to 50% (at 6 months) in age-matched APP-KI mice (Fig. 1C). Notably, HFD slightly exacerbated the age-related increase in LD accumulation, particularly in the APP-KI mice, as the LD$^+$ microglial frequency reached 60% at 6 months in these animals (Fig. 1C and fig. S2). Similarly, the LD area within the microglia increased significantly with age, particularly in the AD model mice (Fig. 1D and fig. S2). These results indicate that microglia accumulate LDs over time and during AD progression, especially under HFD conditions. LDs were also detected inside CD206$^+$ BAMs (Fig. 1E). The percentage of LD$^+$ BAMs and the LD area significantly increased by 6 months of age in both WT and APP-KI groups (Fig. 1, F and G, and fig. S2).

Immunofluorescence staining of diseased murine brain sections revealed the spatial distribution of LD$^+$ microglia in situ. Costaining for IBA$^+$ microglia and LDs (with an anti-IBA antibody and LipidSpot 610, respectively) revealed increased LD accumulation in the microglia surrounding Aβ plaques (Fig. 1H). Approximately 65% of LDAM were localized near the Aβ plaques (Fig. 1I), emphasizing a spatial association between the LDs and Aβ plaques in the AD brain. Notably, LDs were also detected within CD206$^+$ BAMs of the dura mater and subdural meninges (Fig. 1J).

To further investigate the difference in lipid metabolites within the microglia obtained from WT and AD brains, we isolated and sorted microglia from 6-month-old WT and age-matched APP-KI mice. Three independent microglia samples in each group of mice were then subjected to lipidomic analysis (Fig. 2A). Principal component analysis (PCA) revealed the distinct lipid profiles of the microglia in each group, implying that the lipid composition of these subsets was altered during disease progression (Fig. 2B). The levels of glycerolipids increased markedly in the microglia of APP-KI mice (Fig. 2C). Specifically, the primary up-regulated lipid metabolites were triglycerides (TGs) and cholesterol esters (CEs) (Fig. 2D), the main components of LDs. This observation highlights a profound remodeling of microglial lipid composition during AD progression, with enrichment in TGs and CEs.

Pronounced lipid-associated signature in CD11c$^+$ microglia and CD206$^+$ BAMs

We next examined microglia and CD206$^+$ BAMs isolated from 6-month-old WT and AD murine brains using single-cell RNA sequencing (scRNA-seq) to characterize the specific transcriptional signatures of these heterogeneous brain-resident macrophage subpopulations (Fig. 3A). Unsupervised clustering using the uniform manifold approximation and projection (UMAP) method revealed 10 discrete microglial clusters, each representing a unique

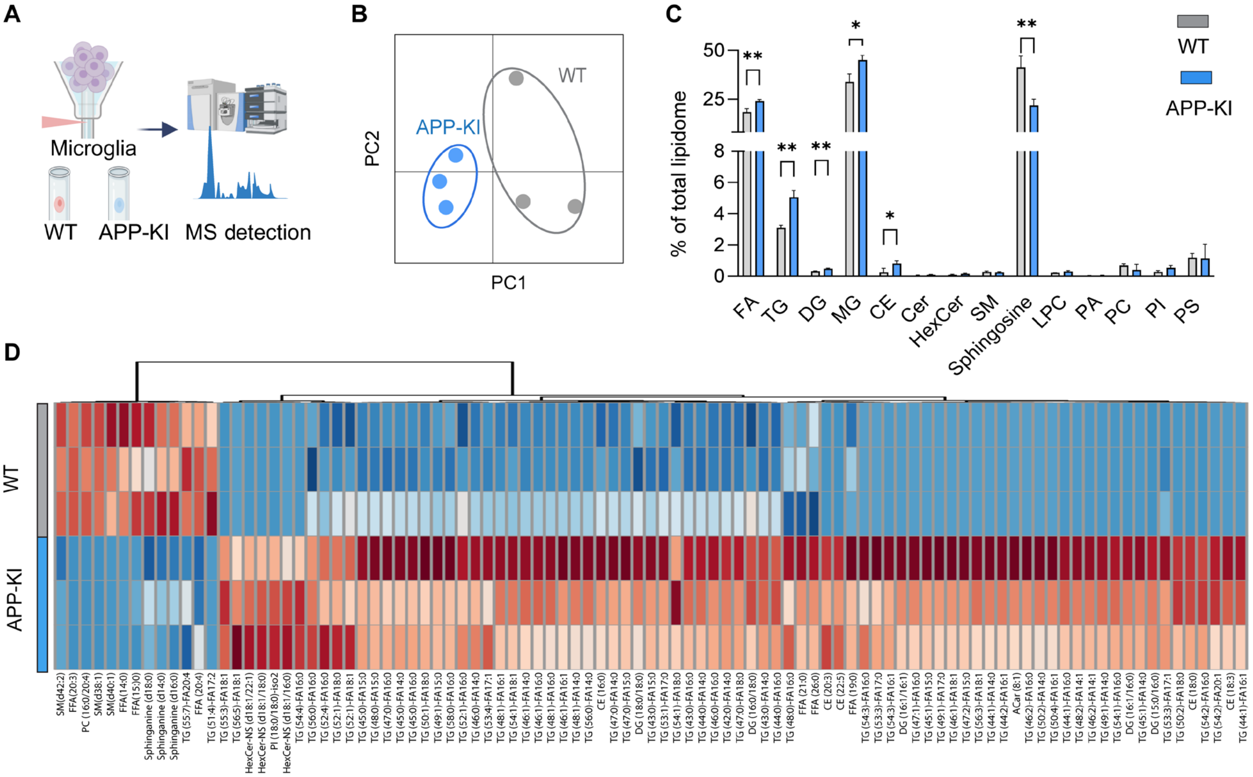

Fig. 2. Lipidomic signature shift in microglia from APP-KI mice. (**A**) Schematic diagram showing the experimental design (image created with BioRender.com). (**B**) 2D PCA plots depicting distinct lipid metabolite profiles of microglia isolated from 6-month-old HFD-fed WT and APP-KI mice. For each data point, sorted microglia (2×10^5 cells) were obtained from a pool of two to three mouse brains. (**C**) Bar chart showing the percentages of distinct lipid categories detected in microglia isolated from WT and APP-KI mice. Lipid categories were classified according to the LIPID MAPS Structure Database (www.lipidmaps.org/databases/lmsd/browse). FA, fatty acyl; DG, diglyceride; MG, monoglyceride; Cer, ceramide; HexCer, hexosylceramide; SM, sphingomyelin; LPC, lysophosphatidylcholine; PA, phosphatidic acid; PC, phosphatidylcholine; PI, phosphatidylinositol; PS, phosphatidylserine. (**D**) Hierarchical clustering heatmap revealing major alterations in lipid metabolites in microglia from WT and APP-KI mice. Samples were analyzed by two-way ANOVA. $^*P < 0.05$; $^{**}P < 0.01$. For clarity, nonsignificant values are not shown.

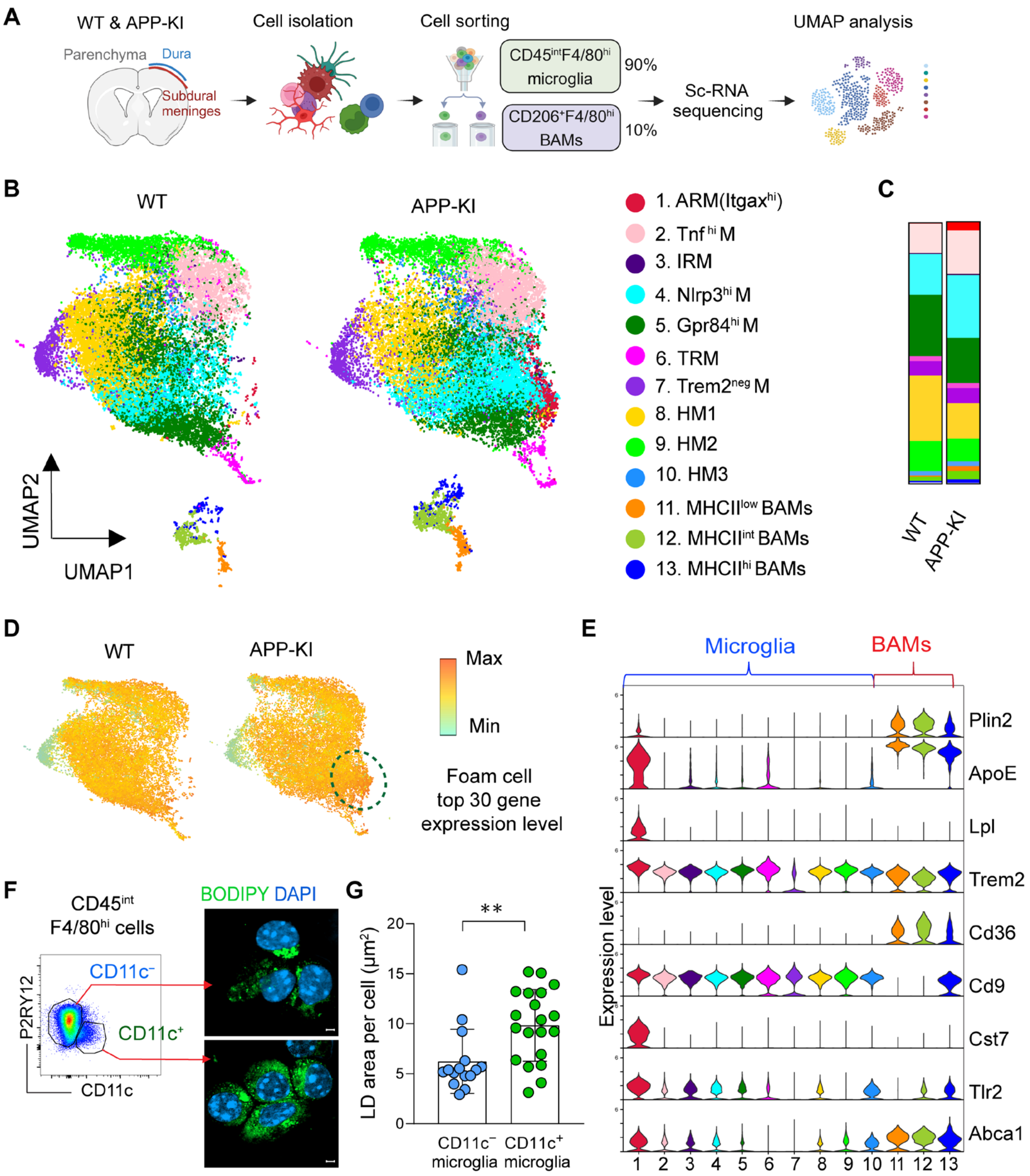

Fig. 3. scRNA-seq reveals a pronounced lipid signature in the CD11c-expressing microglia. (**A**) Schematic diagram showing the experimental design (image created with BioRender.com). Parenchyma and brain borders were processed separately, and obtained microglia and BAMs were sorted and pooled in a ratio of 9 to 1. For each experimental group, sorted microglia and BAMs were obtained from a pool of three mouse brains. (**B**) UMAP plot showing all single-cell data obtained from 6-month-old HFD-fed WT and APP-KI mice that passed quality control. HM1-3, homeostatic microglia 1-3; ARM (Itgax^{hi}), activated-response microglia; TRM, transiting-response microglia; IRM, interferon-response microglia; Nlrp3^{hi}, Nlrp3^{hi} microglia; Gpr84^{hi}, Gpr84^{hi} microglia; Tnf^{hi}, Tnf^{hi} microglia; Trem2^{neg}, Trem2-negative microglia. (**C**) Percentage of each cell cluster identified in the WT and APP-KI groups of mice. (**D**) UMAP plots displaying the average expression levels of the top 30 genes expressed by the foam cell cluster identified in (*5*) in WT and APP-KI mice. (**E**) Violin plots showing the expression levels of genes related to lipid metabolism in each cluster. (**F**) Representative confocal images showing DAPI (blue) and BODIPY (green) staining of sorted CD11c$^+$ and CD11c$^-$ microglia from 6-month-old HFD-fed APP-KI mice. Scale bars, 2 μm. (**G**) Bar chart (with individual values shown as dots) of the LD areas of CD11c$^-$ microglia and CD11c$^+$ microglia. Each dot represents the average result calculated from one slide; three to five slides were evaluated per mouse with $n = 3$ mice per group. Samples were analyzed by Student's *t* test. $^{**}P < 0.01$.

microglial state, and 3 distinct clusters of CD206$^+$ BAMs, with various major histocompatibility complex II (MHCII) expression levels (Fig. 3B). The results showed that AD progression was associated with the expansion of distinct clusters of reactive microglia, such as activated response CD11c$^+$ microglia (ARM), Nlrp3$^+$ inflammasome–related microglia, and Tnf^{hi} microglia (Fig. 3C); of these, the CD11c$^+$ ARM cluster was the most abundant in the brains of AD model mice.

Having observed the presence of LDAM in the mouse AD brain, we next sought to determine whether certain microglial clusters had similar transcriptome profiles to foam cells, the well-characterized, lipid-rich macrophages found near the atherosclerotic plaques (a hallmark of cardiovascular disease). To this end, we analyzed the expression of the top 30 genes recently shown to be enriched in the foam cells of mice with atherosclerosis (*5*). The results revealed enrichment in foam cell–associated genes implicated in lipid metabolism, including

Plin2, *Apoe*, *Trem2*, *Lpl*, and *Cd9*, within the CD11c$^+$ ARM cluster (Fig. 3, D and E). To validate these results, we sorted CD11c$^+$ microglia and CD11c$^-$ microglia and performed BODIPY staining to compare LD levels using confocal microscopy. Our analysis revealed a higher accumulation of neutral lipids within the CD11c$^+$ fraction than their CD11c$^-$ counterparts (Fig. 3, F and G). Notably, CD206$^+$ BAMs also exhibited expression of key genes associated with lipid metabolism (e.g., *Plin2*, *Apoe*, *Trem2*, and *Cd36)* (Fig. 3E), further suggesting their role in lipid storage and metabolism.

Loss of FIT2 reduces the LD load in microglia and CX3CR1$^+$ BAMs

Many studies have demonstrated a phagocytosis defect associated with LD accumulation in microglia (*11*, *13*). We observed a similar inverse correlation between LD content and phagocytic activity when comparing microglia isolated from age-matched WT and APP-KI mice (fig. S3, A to F). Hence, we next sought to explore whether inhibiting LD formation in microglia could restore their phagocytic function. FIT2, a ubiquitously expressed protein, plays a key role in LD biogenesis by facilitating LD formation from the endoplasmic reticulum (*1*). We observed increased *Fit2* mRNA expression in microglia isolated from the brains of AD versus healthy mice (fig. S4A). Given the high expression of CX3CR1 in microglia and BAMs (fig. S4B), we next crossed the $Cx3cr1^{CreERT2}$ mouse strain with the $Fit2^{fl/fl}$ mouse strain (*24*) to generate an inducible $Fit2^{i\Delta M\varphi}$ mouse strain. This mouse strain was characterized by FIT2 depletion specifically in the CX3CR1$^+$ macrophages. To study the role of LDAM in the context of AD, we also crossed the $Fit2^{i\Delta M\varphi}$ strain with the APP-KI strain. To induce FIT2 depletion, the mice in the experimental group were administered 4 mg of tamoxifen (TAM) per day for four consecutive days at 2 months of age, while the control group remained TAM free (Fig. 4A). We observed a substantial depletion in microglial *Fit2* expression at both the genomic and mRNA levels after TAM administration to APP-KI/$Fit2^{i\Delta M\varphi}$ mice (fig. S4, C and D), which was not observed in TAM-injected control $Fit2^{wt/wt}$ $Cx3cr1^{CreERT2}$APP-KI mice (fig. S4C). Other enzymes involved in lipid biogenesis (e.g., Lpin1, DGAT1, and DGAT2) were not altered after CX3CR1-mediated FIT2 depletion (fig. S4E). This setup enabled us to investigate the impact of reduced FIT2 expression on LD formation and, consequently, microglial function in the context of AD.

To determine whether FIT2 deficiency affected the ability of microglia to accumulate LDs, we isolated cells from 6-month-old TAM-treated and untreated APP-KI/$Fit2^{i\Delta M\varphi}$ mice and subjected them to BODIPY staining (Fig. 4A). Notably, the FIT2-depleted microglia of the TAM-treated mice had significantly lower LDs levels than the WT counterparts. The LD area in microglia decreased by ~30% in the absence of FIT2 (Fig. 4, B and C). No LD differences were found in microglia isolated from TAM-treated control $Fit2^{wt/wt}$ $Cx3cr1^{CreERT2}$APP-KI mice, which excluded any TAM-related interference (fig. S5). We also stained brain tissues from 6-month-old TAM-treated and untreated APP-KI/$Fit2^{i\Delta M\varphi}$ mice with LipidSpot

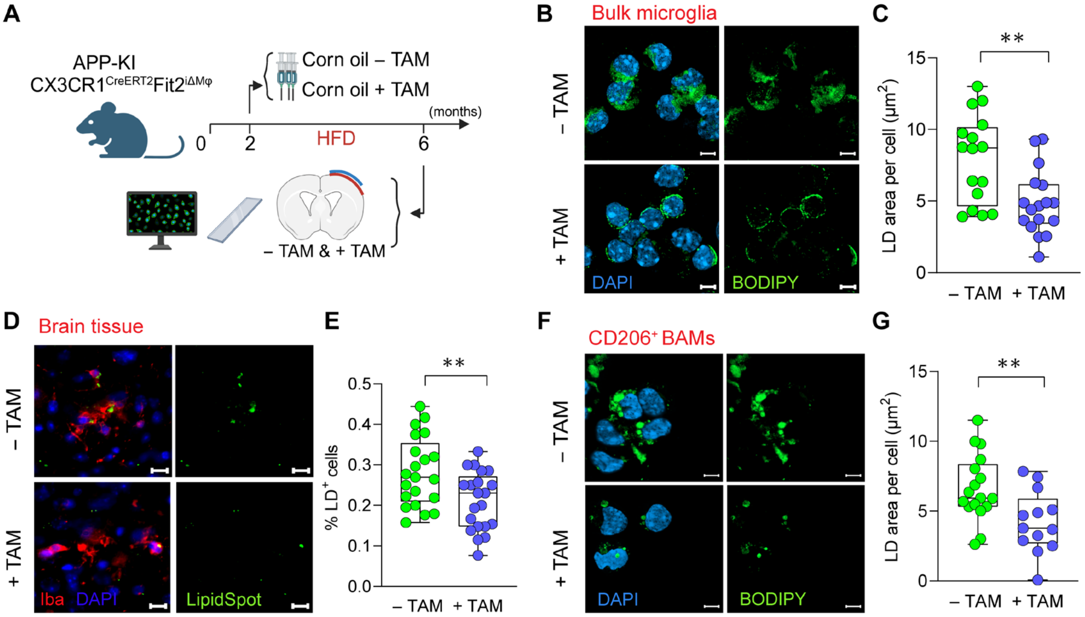

Fig. 4. FIT2-deficient microglia and CD206$^+$ BAMs accumulate fewer LDs. (**A**) Schematic layout showing the experimental design (image created with BioRender.com). (**B**) Representative confocal images of bulk microglia isolated from 6-month-old HFD-fed TAM-treated and untreated APP-KI/$Fit2^{i\Delta M\varphi}$ mice stained with BODIPY (green) and DAPI (blue). Scale bars, 5 μm. (**C**) Quantification of the LD area in microglia from TAM-treated and untreated APP-KI/$Fit2^{i\Delta M\varphi}$ mice. Each dot represents the average result calculated from one slide; three to five slides were evaluated per mouse with $n = 4$ mice per group. (**D**) Representative images showing DAPI (blue), anti-Iba antibody (red), and LipidSpot 610 (green) staining of brain tissue sections from 6-month-old HFD-fed TAM-treated and untreated APP-KI/$Fit2^{i\Delta M\varphi}$ mice. Scale bars, 10 μm. (**E**) Bar charts (with individual values shown as dots) of the percentage of LD$^+$ microglia obtained from TAM-treated and untreated APP-KI/$Fit2^{i\Delta M\varphi}$ mice. Each dot represents the average result calculated from one slide; three to five slides were evaluated per mouse with $n = 5$ mice per group. (**F**) Representative images showing CD206$^+$ BAMs isolated from 6-month-old HFD-fed TAM-treated and untreated APP-KI/$Fit2^{i\Delta M\varphi}$ mice, stained with DAPI (blue) and BODIPY (green). Scale bars, 5 μm. (**G**) Quantification of the LD$^+$ area in CD206$^+$ BAMs obtained from TAM-treated and untreated APP-KI/$Fit2^{i\Delta M\varphi}$ mice. Each dot represents the average result calculated from one slide; three to five slides were evaluated from a sample of three pooled mice with $n = 6$ mice per group. Samples were analyzed using Student's *t* test. $^{**}P < 0.01$.

610 to visualize their microglial LD content in vivo. Consistent with the BODIPY staining results, there was a noticeable reduction in LDAM in the brain tissue of the TAM-treated versus untreated groups (Fig. 4, D and E), indicating that FIT2 deficiency in microglia disrupts their ability to form LDs. As most CD206$^+$ BAMs express high levels of CX3CR1, their LD area was also reduced after FIT2 depletion (Fig. 4, F and G).

Perturbed lipidomic and transcriptomic profiles in FIT2$^{-/-}$ microglia

To further assess the effect of FIT2 deficiency on microglia, we conducted a lipidomic analysis to examine the differences in lipid metabolites between FIT2-depleted and WT microglia of APP-KI mice. The three-dimensional (3D) PCA plot revealed clear distinctions between the lipid profiles of these two groups (Fig. 5A).

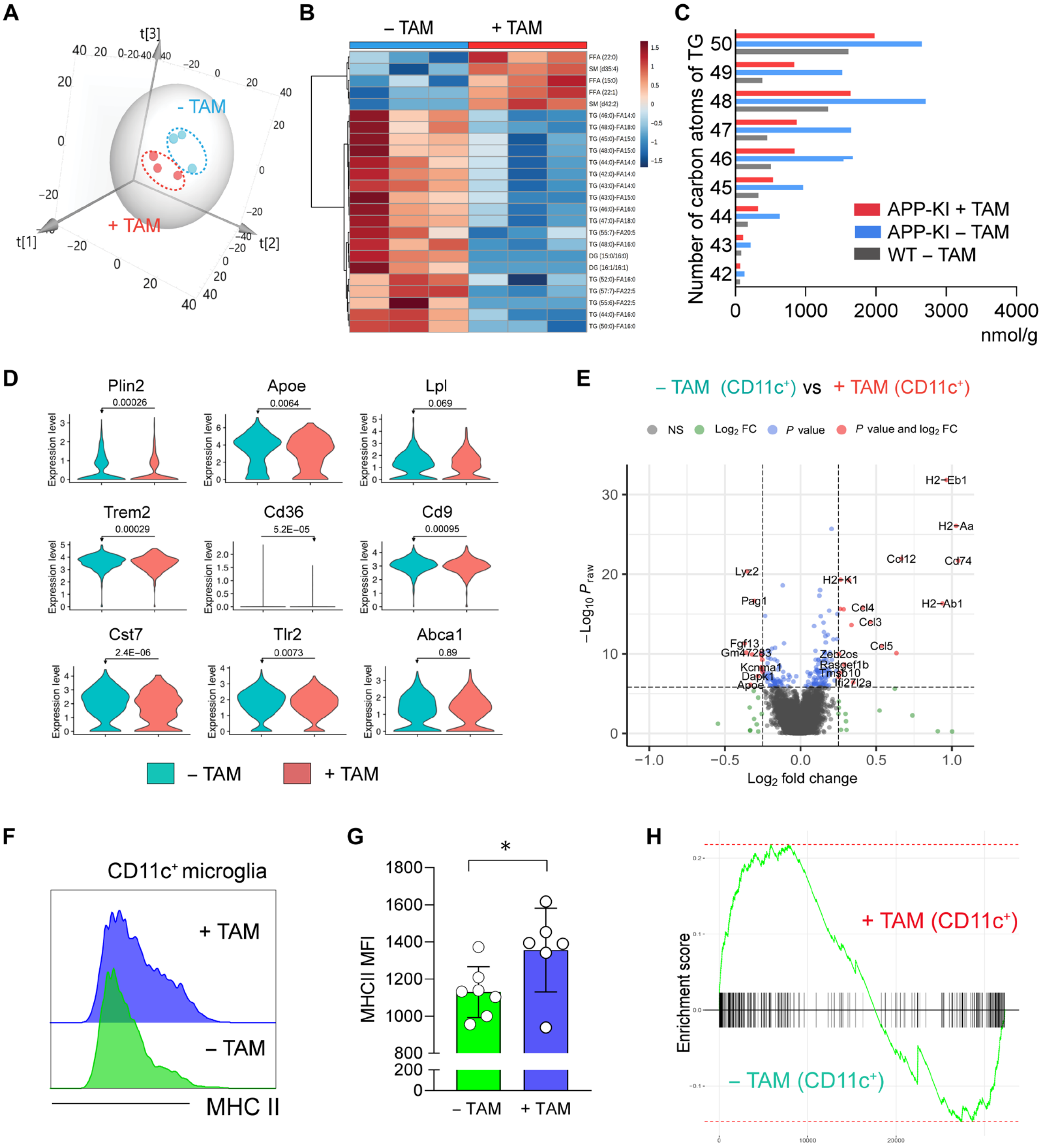

Fig. 5. FIT2 depletion alters the lipidomic and transcriptomic profiles of microglia in the AD brain. (**A**) 3D PCA plot showing the distinct lipid metabolite profiles of microglia isolated from 6-month-old HFD-fed TAM-treated and untreated APP-KI/*Fit2*$^{i\Delta M\varphi}$ mice. For each data point, sorted microglia (2×10^5 cells) were obtained from a pool of two to three mouse brains. (**B**) Hierarchical clustering heatmap showing major alterations in lipid metabolites in microglia from TAM-treated and untreated groups. (**C**) Bar chart showing changes in the levels of different TGs among the microglia isolated from 6-month-old HFD-fed WT, APP-KI, and APP-KI FIT2$^{-/-}$ mice. (**D**) Violin plots showing the expression levels of lipid metabolism–related genes in CD11c$^+$ microglia isolated from TAM-treated and untreated mice. Microglia were sorted from a pool of three mouse brains for each experimental group, as indicated in the figure legend. (**E**) Volcano plot displaying the distinct gene expression profiles of CD11c$^+$ microglia isolated from the TAM-treated and untreated mice. (**F**) Flow cytometry histograms showing the MHCII expression levels of CD11c$^+$ microglia isolated from TAM-treated and untreated mice. (**G**) Bar chart (with individual values shown as dots) showing the mean fluorescence intensity (MFI) of MHCII. Each dot represents a value obtained from one mouse brain and $n = 6$ mice per group. (**H**) Gene set enrichment analysis of lysosomal and phagosomal pathways of CD11c$^+$ microglia isolated from TAM-treated and untreated mice. Samples were analyzed using Student's *t* test. $^*P < 0.05$.

Notably, TG levels were lower in the microglia on TAM-treated than untreated APP-KI/*Fit2*$^{i\Delta M\varphi}$ mice (Fig. 5B and fig. S6). Specifically, the levels of TGs that are typically abundant in the microglia of AD brains (e.g., those containing 46, 48, or 50 carbon atoms) were reduced after TAM administration (Fig. 5C). These findings further support the notion that FIT2 deficiency disrupts microglial lipid metabolism.

Given the alterations in lipid metabolism revealed by LD staining and lipidomic analysis of FIT2-deficient microglia, we next sought to understand the changes in their transcriptomic profile. To this end, microglia and CD206$^+$ BAMs from TAM-treated APP-KI/*Fit2*$^{i\Delta M\varphi}$ mice were isolated and examined by scRNA-seq alongside cells obtained from aged-matched FIT2-WT healthy and AD mice. Given its pronounced lipid-related gene signature, the CD11c$^+$ ARM cluster was characterized in detail. Our results showed that FIT2 deficiency induced subtle yet significant perturbations in the expression of lipid-related genes (e.g., *Plin2* and *Apoe*) within the CD11c$^+$ microglia (Fig. 5D). In addition, genes associated with MHCII presentation, such as *Cd74*, *H2-Aa*, and *H2-Eb1*, were markedly up-regulated in the FIT2-deficient CD11c$^+$ microglia (Fig. 5E); this result was further validated using flow cytometry (Fig. 5, F and G). Given the professional phagocytic nature of microglia, we next performed gene set enrichment analysis and found that the FIT2-depleted CD11c$^+$ microglia were slightly enriched in the lysosomal and phagosomal pathways, indicating that these cells had a higher phagocytic potential than their WT counterparts (Fig. 5H). Although MHCII expression was elevated in FIT2-deficient CD11c$^+$ microglia, quantitative polymerase chain reaction (qPCR) validation showed no significant difference in the pro-inflammatory signature [e.g., interleukin-1α (IL-1α), IL-1β, and IL-6] between FIT2-deficient and WT microglia (fig. S7). Together, these results suggest that FIT2 depletion induces a shift in the lipidomic and transcriptomic profiles of microglia, which may also be associated with alterations in their function.

FIT2 deficiency increases the phagocytic activity of microglia and BAMs

To determine whether the microglial phagocytic function improved after a reduction in their LD content, we next analyzed their phagocytic capacity in vitro. Cells were isolated from the brains of 6-month-old TAM-treated and age-matched untreated APP-KI/*Fit2*$^{i\Delta M\varphi}$ mice. The sorted microglia were then incubated with either pHrodo-labeled *Escherichia coli* bioparticles or Alexa Fluor 647–labeled Aβ oligomers, and phagocytosis was evaluated using fluorescence microscopy and flow cytometry (Fig. 6A). Microscopy revealed an increase in the percentage of *E. coli*$^+$ cells in the FIT2-deficient bulk microglial population (Fig. 6, B and C); this observation was validated by flow cytometry for both the CD11c$^-$ and CD11c$^+$ microglial subsets (Fig. 6, D and E). Phagocytosis assay conducted with Aβ oligomers showed a similar trend, with a significant increase in Aβ$^+$ CD11c$^-$ and CD11c$^+$ microglia observed in the FIT2-deficient group (Fig. 6, F and G). In the case of CD206$^+$ BAMs obtained from TAM-treated APP-KI/*Fit2*$^{i\Delta M\varphi}$, only the two subsets showing the highest levels of CX3CR1 expression (i.e., CD206$^+$MHCII^{hi} and CD206$^+$MHCII^{int}; fig. S4B) exhibited superior phagocytic activity after FIT2 depletion (Fig. 6, H to K). As a control, we also showed that the phagocytic activity of CX3CR1$^-$ neutrophils was not significantly different between the TAM-treated and untreated groups of APP-KI/*Fit2*$^{i\Delta M\varphi}$ mice (fig. S8). These in vitro findings collectively indicate that FIT2 depletion promotes the phagocytic capacity of CD11c$^-$ microglia, CD11c$^+$ microglia, and CD206$^+$ MHCII$^{hi/int}$ BAMs.

Microglial FIT2 deficiency reduces Aβ load in the AD brain

Microglia play a crucial role in clearing Aβ plaques in the brain during AD progression (*25*, *26*). Having demonstrated that FIT2 deficiency increased the phagocytic activity of microglia in vitro, we next assessed the effect of FIT2 depletion on the capacity of microglia to phagocytose Aβ fibrils in vivo. To this end, mice were intraperitoneally injected with methoxy-XO4, a fluorescent probe capable of crossing the blood-brain barrier to stain Aβ (Fig. 7A). Microglia were harvested at 3 hours after injection, and the proportion of methoxy-XO4$^+$ cells was determined by flow cytometry. We observed an increase in the rate of Aβ uptake and phagocytosis by microglia (especially the CD11c$^+$ subset) after the FIT2-associated reduction in LD load (Fig. 7, B and C). We continued to investigate Aβ deposition in the brain tissue of TAM-treated and untreated APP-KI/*Fit2*$^{i\Delta M\varphi}$ mice by performing Aβ immunofluorescence staining of brain sections, focusing specifically on the cortex and hippocampus (Fig. 7D). An anti-Aβ monoclonal antibody (82E1) and the thioflavin S (ThioS) dye were used to detect Aβ plaques and fibrils in brain tissue (Fig. 7E). Analysis of several brain sections from distinct TAM-treated and untreated mice revealed significantly lower levels of Aβ plaque deposition in the hippocampus and cortex of the FIT2-deficient versus WT groups of mice (Fig. 7, F and G). To further investigate the impact of reduced microglial lipid load on neuroinflammation, we collected one hemisphere from each brain to assess inflammatory cytokine and chemokine RNA levels. Our results revealed a reduction in key pro-inflammatory molecules, including *Tnfa*, *Il6*, *Ccl2*, and *Ccl4*, in FIT2-deficient APP-KI mice (fig. S7). These results suggest a correlation between microglial LD load and Aβ plaque accumulation, implying that modulating the microglial function could be a potential strategy for mitigating Aβ pathology and neuroinflammation in AD.

FIT2 depletion increases the efferocytic activity of microglia

Microglia also contribute to the maintenance of brain homeostasis by clearing apoptotic cells in the brain via efferocytosis (*27*–*29*). Microglial efferocytosis relies on many features of phagocytosis such as the ability to recognize, engulf, digest, and dispose of apoptotic cells and other cellular waste materials (*29*). Having shown that the reduction in LD content increased the phagocytic activity of microglia, we next investigated whether it similarly affected their efferocytic activity. To this end, Neuro 2a (N2A) cells were stained with CellTracker CMFDA dye and treated with 1 mM H_2O_2 for 20 hours to induce cell apoptosis. Microglia isolated from the TAM-treated and untreated APP-KI/*Fit2*$^{i\Delta M\varphi}$ mice were then incubated with the apoptotic N2A cells for 2 hours. Last, flow cytometry was used to determine the percentage of CMFDA$^+$ microglia as an indicator of their efferocytosis activity (fig. S9A).

The results showed that although both CD11c$^-$ microglia and CD11c$^+$ microglia ingested apoptotic N2A cells, their efferocytic capacity increased after TAM treatment, indicating that FIT2 deficiency promoted efferocytosis (fig. S9, B and C). These findings suggest that the reduction in LD levels within microglia positively correlates with their efferocytic activity, emphasizing the potential impact of lipid metabolism on the microglial function that is critical for maintaining brain homeostasis.

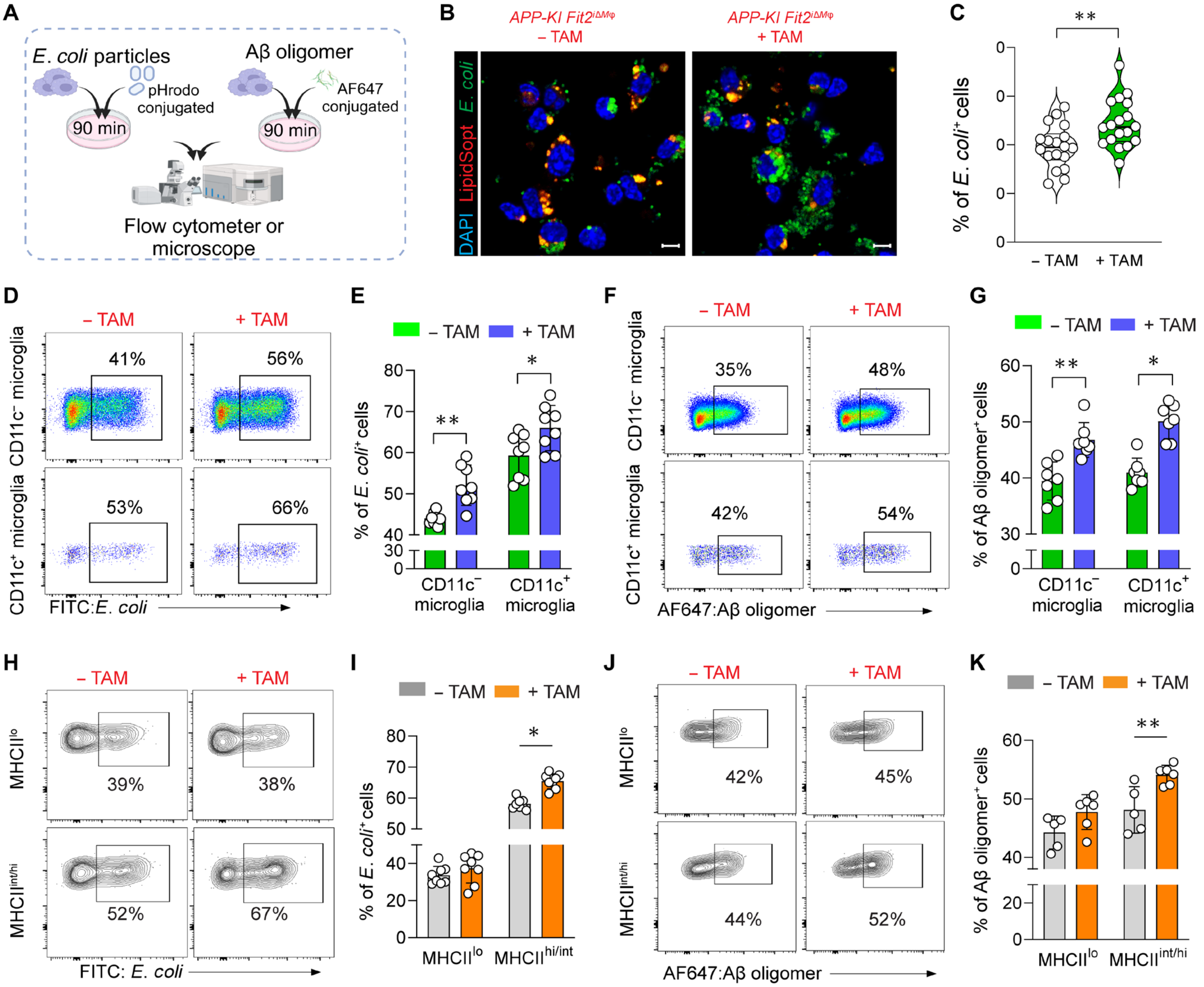

Fig. 6. FIT2 deficiency increases the phagocytic activity of microglia and BAMs. (**A**) Schematic layout showing the experimental design (image created with BioRender.com). AF647, Alexa Fluor 647. (**B**) Representative images showing microglia isolated from 6-month-old HFD-fed TAM-treated and untreated APP-KI/*Fit2*$^{i\Delta M\varphi}$ mice stained with LipidSpot 610 (red), DAPI (blue), and engulfment of *E. coli* bioparticle (green). Scale bars, 10 μm. (**C**) Bar chart of the percentages of *E. coli*$^+$ microglia in TAM-treated and untreated APP-KI/*Fit2*$^{i\Delta M\varphi}$ mice. Each dot represents the average result calculated from one region of interest; five to seven regions of interest were evaluated per mouse with $n = 5$ mice per group. (**D** and **E**) Flow cytometry plots and bar chart displaying the percentages of *E. coli*$^+$ CD11c$^-$ and CD11c$^+$ microglia isolated from TAM-treated and untreated APP-KI/*Fit2*$^{i\Delta M\varphi}$ mice. Each dot in the bar chart represents the result obtained from one mouse and $n = 8$ mice per group. (**F** and **G**) Flow cytometry plots and bar chart displaying the percentages of Aβ oligomer$^+$ CD11c$^-$ and CD11c$^+$ microglia isolated from TAM-treated and untreated APP-KI/*Fit2*$^{i\Delta M\varphi}$ mice. Each dot in the bar chart represents the result obtained from one mouse and $n = 7$ mice per group. (**H** and **I**) Flow cytometry plots and bar graph showing the percentages of *E. coli*$^+$ MHCII$^{hi/int}$ BAMs and MHCII^{lo} BAMs isolated from TAM-treated and untreated mice. Each dot represents the percentage of *E. coli*$^+$ cells obtained from one mouse brain and $n = 8$ mice per group. (**J** and **K**) Flow cytometry plots and bar graph showing the percentages of Aβ oligomer$^+$ MHCII$^{hi/int}$ BAMs and MHCII^{lo} BAMs isolated from TAM-treated and untreated mice. Each dot in the bar chart represents the percentage of Aβ$^+$ cells obtained from one mouse brain and $n = 5$ to 6 mice per group. Samples were analyzed by Student's *t* test (C) and two-way ANOVA [(E), (G), (I), and (K)]. $^*P < 0.05$; $^{**}P < 0.01$. For clarity, nonsignificant values are not shown.

DISCUSSION

Numerous studies have highlighted the crucial contribution of microglia to brain homeostasis during aging and neurodegeneration (*17*, *18*, *28*, *30*). These studies have revealed the existence of diverse microglial phenotypes and their varied activation states and functions in response to age- or disease-dependent inflammation. The present study provides insights into how LD-loaded brain macrophages are influenced by age, disease state, and diet. For instance, we confirmed the findings of Marschallinger *et al.* by showing that LDAM numbers increased with age (*11*). In addition, we demonstrate that microglial LD content not only was slightly enhanced under obese conditions, but was considerably accelerated during AD development in a diet-independent manner. Specifically, we showed that CD11c$^+$ microglia located near Aβ plaques in the AD brain progressively accumulated more LDs. In addition, we confirmed previous findings of elevated expression of lipid-related genes in BAMs (*31*) and observed an increase in LD content within these cells over time and during disease progression. Given that LD accumulation in

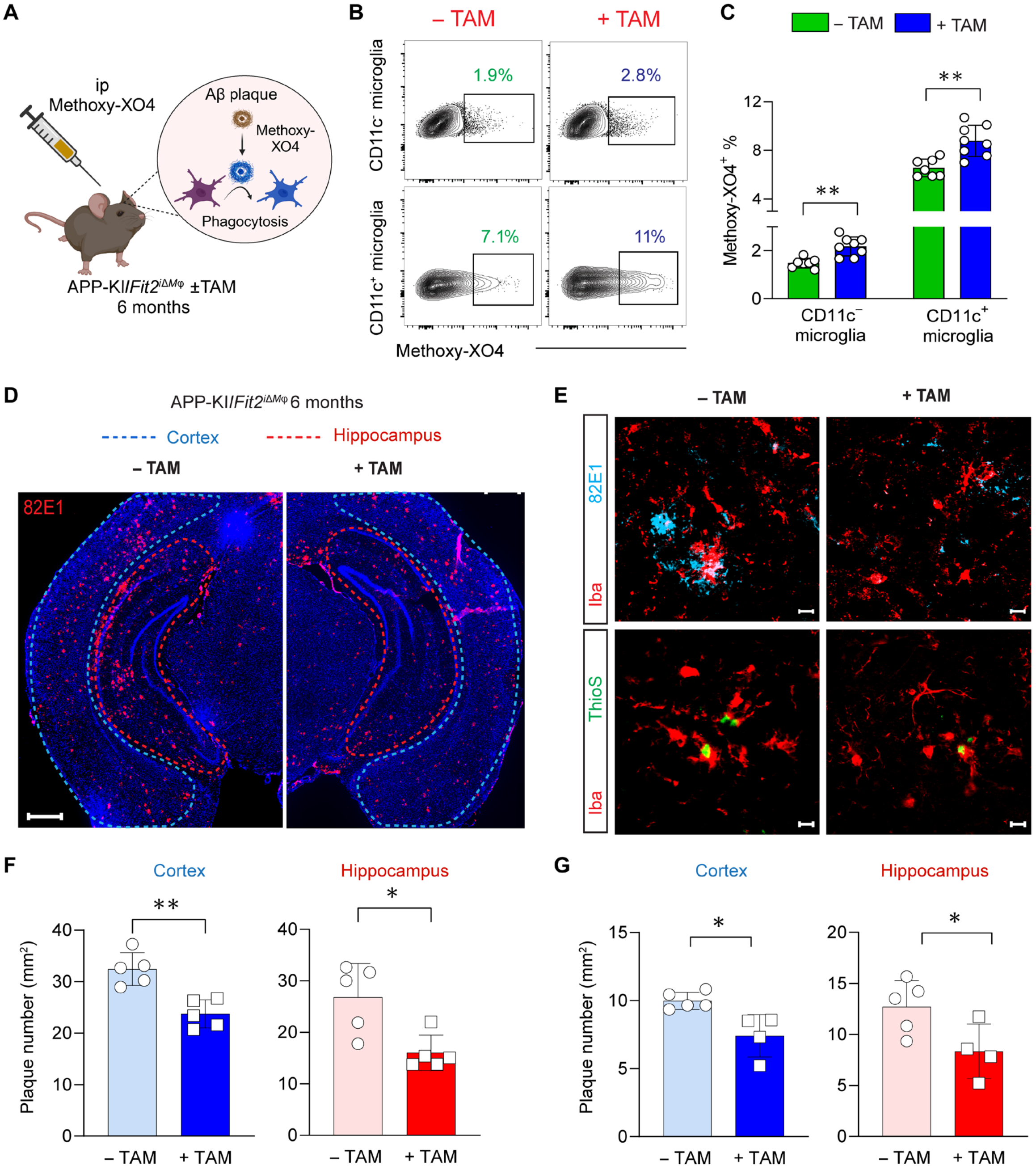

Fig. 7. Microglial FIT2 deficiency reduces Aβ load in the AD brain. (**A**) Diagram illustrating the use of methoxy-XO4 in the in vivo phagocytosis assay (image created with BioRender.com). ip, intraperitoneally. (**B**) Representative flow cytometry plots displaying the methoxy-$XO4^+$ $CD11c^-$ and $CD11c^+$ microglia isolated from 6-month-old HFD-fed TAM-treated and untreated APP-KI/*Fit2*$^{i\Delta M\varphi}$ mice. (**C**) Bar chart (with individual values shown as dots) of the percentage of methoxy-$XO4^+$ $CD11c^-$ and $CD11c^+$ microglia isolated from TAM-treated and untreated mice. Each dot represents the result obtained from one mouse brain and $n = 8$ mice per group. (**D**) Representative images showing anti-Aβ antibody (82E1) staining of the brain tissues of TAM-treated and untreated APP-KI/*Fit2*$^{i\Delta M\varphi}$ mice. Scale bar, 100 μm. Blue outline, cortex; red outline, hippocampus. (**E**) Upper panel: Representative confocal images of anti-Aβ (blue) and anti-Iba (red) antibody staining of brain tissues. Scale bars, 10 μm. Lower panel: Representative confocal images of ThioS (green) and anti-Iba antibody (red) staining of brain tissues. Scale bars, 10 μm. (**F**) Quantification of the anti-Aβ antibody–positive plaques in the cortex and hippocampus. Each dot represents the average result obtained from an individual mouse brain with $n = 5$ mice per group. (**G**) Quantification of the ThioS-stained Aβ plaques in the cortex and hippocampus. Each dot represents the average result obtained from an individual mouse brain with $n = 4$ to 5 mice per group. Samples were analyzed by two-way ANOVA (C) and Student's *t* test [(F) and (G)]. $*P < 0.05$; $**P < 0.01$.

LDAM impairs their phagocytic ability, we decided to target FIT2, a key protein involved in LD biogenesis, to inhibit LD formation and potentially restore the phagocytic function. We showed that FIT2 depletion in microglia lowered their LD loads, altered their lipidome and transcriptome signatures, and ultimately improved their ability to Aβ phagocytosis and efferocytosis of apoptotic neurons.

Recent scRNA-seq studies have identified distinct states of microglial activation in brains affected by neurogenerative disease; some of these activation states were characterized by the enrichment in genes involved in lipid and lipoprotein metabolism (*14*, *32*), indicating a close relationship between lipid metabolism and microglial activation. The brain is one of the most lipid-rich organs. Brain microglia can increase their intracellular lipid content (*33*) by assimilating lipids (e.g., myelin debris) from their environment (*34*). LD accumulation in macrophages has also been documented in lipid-rich microenvironments in the peripheral, such as atherosclerosis plaques (*5*), white adipose tissue (*10*), and tumors (*9*). In our study, a series of proteins involved in extracellular lipid uptake, such as TREM2 and LPL (*35*), were highly expressed in mRNA in microglia obtained from the AD brain. TREM2 binds to various lipid ligands, such as APOE particles (main cholesterol carriers in the brain) and myelin debris, to mediate lipid sensing and uptake (*36*). Mutations affecting the TREM2 function impair microglial activation (*37*) and reduce their ability to accumulate LDs in the AD brain (*38*). In addition, we demonstrated the accumulation of LDAM around Aβ plaques in the AD brain. These LDAM had an elevated LD load and overexpressed genes related to lipid metabolism. By removing Aβ aggregates via TREM2 and other phagocytic receptors (e.g., AXL), the microglia located near Aβ plaques provide a protective barrier that limits plaque formation (*14*). A recent study demonstrated that primary microglia undergo profound lipidome perturbations to promote LD formation upon exposure to Aβ aggregates (*39*). Moreover, we found that genes encoding Toll-like receptors (TLRs) such as *Tlr2*, which participates in Aβ recognition in the brains of AD model mice (*40*, *41*), were up-regulated in the CD11c$^+$ microglia. Comparable innate responses induced by lipopolysaccharide have been strongly linked to LD formation within microglia (*11*). In accordance, TLR2 inhibition has been shown to markedly mitigate lipopolysaccharide-induced lipid accumulation in hepatic cells (*42*). These reports further imply that Aβ-induced microglial activation also contributes to LD accumulation. The inflammatory activation of microglia triggers their metabolic reprogramming (*43*). Thus, in the AD brain, chronic and Aβ-induced inflammation could promote a sustained metabolic shift from mitochondrial oxidative phosphorylation to glycolysis (*44*), resulting in the excessive formation and accumulation of LDs within microglia. The accumulation of LDs is associated with changes in the lipid profile, particularly an increase in TGs and CEs. In contrast, sphingolipids, particularly sphingosine, were found to be reduced in the diseased microglia. These abnormal changes in sphingolipid levels have been closely linked to neuroinflammatory disorders, as they play a crucial role in cell signaling and are, therefore, frequently discussed as potential therapeutic targets (*45*, *46*).

Phagocytosis is the major mechanism contributing to Aβ aggregate clearance in the brain, with microglia serving as the main effector cells for engulfing and degrading Aβ (*30*). However, we and others (*11*, *13*, *39*) have observed that excessive LD accumulation within microglia led to a decline in their phagocytic activity, potentially reducing the efficiency of Aβ clearance in the AD brain. The decreased phagocytic activity also results in the insufficient clearance of apoptotic cells (efferocytosis) in the brain; the release of intracellular content from dead and dying cells, in turn, induces secondary necrosis and inflammation, which exacerbates disease pathology (*47*). Exactly how LD accumulation affects the phagocytic capacity of macrophages remains elusive. Intracellular compartment interactions between LDs and lysosomes or between LDs and mitochondria may play a role in this process. Intracellular LDs within macrophages are transported to lysosomes for enzymatic degradation in a process called lipophagy (*48*). A recent study highlighted close contact between LDs and lysosomes within microglia, suggesting that, in LDAM, lysosomes might be used for lipophagy rather than the degradation of phagocytosed material (*11*). LD overload could also induce lysosomal defects (*49*), ultimately leading to phagocytosis impairment. Moreover, increased lipid accumulation promotes fatty acid oxidation and ROS production, leading to mitochondrial damage (*50*) and phagocytosis inhibition (*51*); these defects can be mitigated by mitochondrial transplantation (*52*). Furthermore, in microglia, small LDs can interfere with structural filaments, leading to cytoskeletal dysfunction and reduced phagocytic activity (*53*).

Many studies have underscored the therapeutic importance of restoring microglial phagocytosis (*54*–*56*). Given the dysfunctional phenotype observed in LDAM, we next investigated whether targeting FIT2, a key protein mediating LD formation, would reduce LDs and restore microglial phagocytosis and efferocytosis in AD (*1*, *57*). Several studies have elucidated the significance of FIT2 in LD biogenesis across various cell types. For instance, in vitro FIT2 overexpression promoted LD accumulation in human embryonic kidney 293 cells, while FIT2 knockdown reduced TG levels and LD accumulation in mouse adipocytes (*58*). The in vivo loss of FIT2 in adipocytes and pancreatic β cells also resulted in failed LD formation (*24*, *59*). In our study, we found that microglia lacking FIT2 had fewer LDs and lower TG levels, suggesting that targeting FIT2 was sufficient to perturb LD formation within microglia. We observed increased rates of *E. coli* bioparticle, Aβ, and apoptotic cell phagocytosis in both the FIT2-deficient bulk and CD11c$^+$ microglia. This was accompanied by the up-regulation of lysosomal and phagosomal pathways, particularly in the FIT2-depleted CD11c$^+$ microglial subset. A similar increase in Aβ phagocytosis was observed in microglia treated with DGAT2 inhibitors, which attenuate TG formation and LD accumulation (*39*). These findings suggest that phagocytosis impairment is a consequence rather than a cause of LD accumulation in the AD brain; thus, targeting LD formation could be used to restore phagocytic activity. In addition, the up-regulation of MHCII expression in FIT2-deficient CD11c$^+$ microglia might be related to their elevated phagocytic activity. MHCII$^+$ microglia exhibited higher rates of phagocytosis than their MHCII$^-$ counterparts in 5xFAD mice (*60*). Similarly, microglia participating in Aβ phagocytosis expressed higher levels of MHCII-related genes (*61*). Our findings suggest that reducing microglial LD load via FIT2 depletion or other pharmacological interventions is a feasible therapeutic strategy for boosting the phagocytic activity of these cells to mitigate Aβ deposition in the brain. In line with this proposed strategy, reversing the lipid-laden phenotype of tumoral macrophages has already been successfully used to suppress the development of gastric cancer (*62*).

While our study reported the detrimental effects of LD accumulation on microglial functionality, some recent studies have demonstrated the neuroprotective roles of LDs in other pathological processes. In ischemic brain injury, for instance, LDs mitigate the microglial pro-inflammatory response, decrease infarct volume, and improve their neurobehavioral performance (*63*, *64*). These conflicting roles of microglial LDs may be due to variations in the type of pathology (acute versus chronic) and the LD content. Unlike in ischemic stroke, where the accumulation of microglial LDs is induced by an acute proinflammatory microenvironment, the accumulation of LDs within microglia reported in our study was induced by chronic inflammation. In relation to LD content, we and others have revealed the presence of more GLs in aged and diseased microglia (*11*), while the macroglia encountered in ischemic stroke are characterized by high cholesterol levels (*63*). Moreover, the initial neuroprotective effect of LDs after injury may gradually become detrimental over time (*13*). Therefore, understanding the impact of LD accumulation on the macrophage function and overall brain health is crucial when designing therapeutic strategies for AD and other neurodegenerative diseases.

The contribution of BAMs to the development of neurodegenerative and neuroinflammatory diseases such as AD is still widely debated but becoming increasingly recognized (*21*, *22*). Depletion of brain and leptomeningeal BAMs in 5xFAD mice has been shown to compromise the glymphatic function and increase Aβ burden in the brain (*23*), suggesting a protective role of BAMs in maintaining brain functions induced by Aβ accumulation and deposition. However, as aging progresses and amyloidosis and/or tauopathy worsen, BAMs may adopt harmful activation profiles that exacerbate microglial overactivation, contributing to excessive synaptic pruning and neuronal dysfunction (*65*). Here, we conducted a pioneering investigation into the lipid-accumulating capacity of BAMs in the context of AD. We demonstrated that CD206$^+$ BAMs had a pronounced lipid-related transcriptomic signature and displayed several lipid-accumulating phenotypes. Given their specific spatial location at the interface between the periphery nervous system and the central nervous system, BAMs may facilitate the storage and transportation of lipids across these regions, contributing to lipid homeostasis in the brain and influencing cellular metabolism within the central nervous system. In situ LipidSpot staining showed that the CD206$^+$ BAMs located in the dura mater and subdural meninges of the brain were also capable of accumulating LDs. The dura mater is considered the epicenter of immune surveillance in the brain, where macrophages present antigens to T cells to induce immune responses (*66*). Excessive LD accumulation within macrophages has been reported to weaken their antigen-presenting activity (*43*), which could result in the dysregulation of brain homeostasis. In addition, BAMs control the neurovasculature, for instance, by mediating arterial motion and driving the flow of cerebrospinal fluid (*23*). LD accumulation in macrophages can elevate their ROS production (*9*, *11*), promoting neurovascular dysfunction (*67*). Moreover, the LD-mediated impairment of BAM phagocytosis may also lead to insufficient waste clearance at the brain interface and in the perivascular space, causing the excessive deposition of debris, such as Aβ (*68*, *69*). In our study, FIT2 depletion effectively impaired LD formation in BAMs and increased their phagocytic activity, suggesting that LD formation/accumulation could be targeted to regulate the functions of BAMs in addition to those of microglia.

Certain limitations to our work will be the focus of future research. First, while we demonstrated that FIT2-deficient microglia exhibited reduced LD content, they were not entirely devoid of LDs. Since FIT2 is primarily involved in TG-mediated LD development (*58*), sterol esters might still contribute to LD formation without this FIT isoform. This may explain why CE levels were not markedly affected in the FIT2-deficient microglia. Second, although the APP-KI mouse model can offer some advantages over the transgenic mouse models that overexpress APP protein, they appeared to display a relatively mild behavioral phenotype (*70*) than other transgenic mouse models, which makes it challenging to assess the significance of this microglial functional restoration in the behavior of APP-KI mice. Third, our study demonstrated that the augmented microglial phagocytosis significantly reduced Aβ in the brain tissue. However, whether Aβ accumulation is involved in AD progression and cognitive decline is still under intense debate (*71*, *72*) since other factors, such as hyperphosphorylated tau protein (*71*, *72*), brain inflammation (*73*), and other yet-to-be-identified mechanisms, can contribute to the initiation and disease development. Therefore, it will be important to explore whether targeting LD load in microglia could also reduce tau deposition or address other misfolded proteins in the brain. Last, our data suggest that LD is a promising target for rewiring microglia phagocytic and efferocytic abilities. Yet, additional studies are needed to determine effective pharmacological interventions targeting LD metabolism and their implications in clinical studies.

In summary, our study underscores the potential of FIT2 depletion in reducing LD accumulation within both microglia and CD206$^+$ BAMs to improve their phagocytic activity in the AD brain. Our findings suggest that strategies aimed at reducing microglial/macrophage LD load hold promise in rewiring their functionality and bolstering their resilience in the context of neurogenerative disorders.

MATERIALS AND METHODS

Experimental design

The primary objective of this study was to investigate the formation of LD-loaded brain macrophages and their implications in the AD mouse model. To this aim, we conducted a comprehensive analysis of LD content within microglia and BAMs obtained from mice under diverse conditions, including various ages, disease states, and dietary interventions. In addition, we used CX3CR1$^+$ macrophage–specific FIT2-deficient mice to explore the characteristics of brain macrophages with reduced LD content in the context of AD. We used lipidomic and scRNA-seq to determine the changes in the lipidome and transcriptome of microglia with FIT2 deficiency. Furthermore, we conducted in vitro and in vivo assays to assess the functional consequence of reduced LD content in microglia. Specifically, we evaluate microglial capacity for Aβ and apoptotic neuron cell clearance.

In the experimental design, animals were randomized into different treatment groups to minimize bias; investigators were not blind to the treatment group, and no values were excluded from the analysis. Each experiment, except scRNA-seq and lipidomic analyses, was repeated at least three times to ensure the reliability of the results. The sample sizes for each experiment are indicated in the figure legend.

Mice

The *App*$^{\text{NL-G-F}}$ (APP-KI) mouse model is a knockin mouse line coexpressing the Swedish (KM670/671 NL), Beyreuther/Iberian [/Iberian (I716F)], and Arctic (E693G) mutations, effectively mimicking AD-associated pathologies such as amyloid plaques, synaptic loss, and microgliosis (*74*). The inducible *Fit2*$^{i\Delta M\varphi}$ mouse strain was generated by crossing with floxed *Fit2* (*Fit2*$^{fl/fl}$) mice (*24*) expressing TAM-inducible Cre-recombinase under the control of the *Cx3cr1* promoter (*Cx3cr1*^{CreERT2}). The inducible *Fit2*$^{i\Delta M\varphi}$ mouse strain was subsequently bred with APP-KI mice, leading to the generation of a new mouse line named APP-KI/$Fit2^{i\Delta M\varphi}$. Some experiments were performed with $Fit2^{wt/wt}$ $Cx3cr1^{CreERT2}$APP-KI mice to exclude any side effects of TAM. All mice included in this study were specifically males, ensuring a standardized and controlled experimental environment. All mice were bred and maintained in a specific pathogen–free animal facility at Nanyang Technological University (Singapore). All animal studies were carried out according to the recommendations of the National Advisory Committee for Laboratory Animal Research, and the A19093 protocol was approved by the Institutional Animal Care and Use Committee of the Nanyang Technological University.

TAM-inducible FIT2 depletion in CX3CR1$^+$ cells

To induce *Fit2* depletion in CX3CR1$^+$ cells, the inducible $Fit2^{i\Delta M\varphi}$ and APP-KI/$Fit2^{i\Delta M\varphi}$ mouse lines were treated with 4 mg of TAM (dissolved in corn oil) per day for four consecutive days via gavage at 2 months of age. Control age-matched $Fit2^{i\Delta M\varphi}$ and APP-KI/$Fit2^{i\Delta M\varphi}$ mice were not subjected to TAM treatment.

Isolation of microglia from the brain parenchyma

Microglia were isolated as previously described (*75*). Briefly, mice were decapitated, and their brains were harvested and digested in Iscove's modified Dulbecco's medium (IMDM) containing 2% fetal bovine serum (FBS), deoxyribonuclease I (Roche, Basel, Switzerland), collagenase D (Roche), and dispase II (Gibco, US). The tissues were then crushed and homogenized using a syringe before being filtered through a cell strainer. Myelin debris and red blood cell contamination were removed on a Percoll (Cytiva, Sweden) gradient and 0.89% NH_4Cl lysis buffer. Last, the cell suspension was collected for further processing.

Flow cytometry and cell sorting

After obtaining a single-cell suspension, the cells were preincubated with anti-Fc receptor antibody (10 μg/ml; clone 2.4G2) on ice for 20 min. Subsequently, the cells were stained with distinct panels of antibodies (also 20 min on ice) diluted in phosphate-buffered saline (PBS) with 2% FBS. After a washing step, the cells were stained with 4′,6-diamidino-2-phenylindole (DAPI; 1:1000, Thermo Fisher Scientific, Waltham, MA) to exclude dead cells. Last, the cells were washed and resuspended in PBS with 2% FBS for acquisition on a BD Symphony A5.2 flow cytometer or for sorting on a BD FACS Aria cell sorter. Data were analyzed using FlowJo software (TreeStar, Ashland, OR). The following antibodies were used for flow cytometry: anti-CD45 (RRID:AB_2873123, BD Biosciences), anti-CD11b (RRID:AB_830642, BioLegend), anti-Ly6C (RRID:AB_2562617, BioLegend), anti-Ly6G (RRID:AB_1236494, BD Biosciences), anti-F4/80 (RRID:AB_893490, BioLegend), anti-CD11c (RRID:AB_2565268, BioLegend), anti-P2RY12 (RRID:AB_2721469, BioLegend), anti-I-A/I-E (RRID:AB_2734168, BioLegend), and anti-CD206 (RRID:AB_2629637, BioLegend).

Cytospinning and LD staining

Sorted cells were resuspended in PBS with 2% FBS at 100,000 cells per 100 μl. The cell suspension (100 μl) was subsequently transferred to a cytofunnel and centrifuged at 300*g* for 3 min onto a cytospin slide. After 2 hours of air-drying at room temperature, cells were fixed with 4% paraformaldehyde (PFA) for 15 min at room temperature.

Two different LD staining procedures were used: BODIPY (Invitrogen, US) was diluted in PBS to a final concentration of 5 μg/ml, while LipidSpot 610 (Biotium, US) was diluted in PBS at a ratio of 1:1000. Subsequently, cells were incubated with either BODIPY or LipidSpot 610 at 37°C for 20 min and then washed three times with 1× PBS. Last, the slides were mounted using a fluorescent mounting medium (Dako, Denmark) containing DAPI. High-resolution images of the stained slide were captured by a Zeiss confocal microscope. The percentage of LD$^+$ cells was calculated manually. The LD load per cell was measured using ImageJ by selecting Analyze > Analyze Particles to evaluate the LD area within each cell.

Perfusion and tissue preparation for immunofluorescence staining

Mice were perfused with 20 ml of 1× PBS before having their brains extracted and postfixed with 4% PFA at 4°C for 24 hours. The tissues were then transferred to a 15% sucrose solution for 24 hours before being immersed in a 30% sucrose solution for an additional 24 hours. After this process, the brains were embedded in the Optimal Cutting Temperature compound (Sakura Finetek, US). Coronal sections (30 μm) were then obtained using a Leica cryostat and were preserved in a cryoprotectant solution (0.1 M phosphate buffer, glycerol, and ethylene glycol at 2:1:1 by volume) at −20°C.

To prepare the dura mater for tissue analysis, the dorsal part of the skull was removed, and the dura mater was carefully peeled off from the skull cap and placed in 2% FBS IMDM. The subdural meninges were then microdissected and placed in ice-cold 2% FBS IMDM. The isolated tissues were postfixed with 4% PFA at 4°C for 1 h, washed three times with 1× PBS, and subjected to immunofluorescence staining.

Immunofluorescence staining

Free-floating brain sections, dura mater, and subdural meninges were washed three times with 1× PBS and then incubated with 5% bovine serum albumin (BSA) for 1 hour. The sections were then stained with primary antibodies (diluted in 5% BSA) at 4°C overnight. Next, the sections were washed three times with 1× PBS and stained with the correspondent secondary antibodies (diluted in 5% BSA). The stained sections were then mounted onto microscope slides, embedded using fluorescent mounting medium (Dako) containing DAPI, and analyzed using a confocal fluorescent microscope (Zeiss). Detailed microscopy image acquisition settings were indicated in the figure legend. Last, the images were processed using Zen and ImageJ software. The following primary and secondary antibodies were used for immunofluorescence staining: anti-Iba-1 (RRID:AB_839504, Fujifilm Wako Shibayagi), anti-CD206 (RRID:AB_10917384, BioLegend), anti-82E1 (RRID:AB_10707424, IBL), anti-Rabbit IgG (RRID:AB_2563202, BioLegend), anti-Rabbit IgG (RRID:AB_2563306, BioLegend), anti-Mouse IgG (RRID:AB_10696420, BioLegend), streptavidin (RRID:AB_10053373, BD Biosciences), and streptavidin (RRID:AB_10054235, BD Biosciences).

To detect LDs within the tissue sections, antibody-stained, free-floating brain sections were incubated with LipidSpot 610 (1:1000) for 20 min at 37°C and then washed three times with 1× PBS. Sections were then mounted onto microscope slides and embedded using a fluorescent mounting medium (Dako) containing DAPI.

Aβ oligomerization

Aβ oligomerization was conducted as previously described (*51*). Briefly, fluorescently labeled Aβ peptides (Aβ 1 to 42, AnaSpec, AS-64161) were dissolved in a 1% NH_4OH solution (40 μl for 0.5 mg of peptide) and then diluted with 1× PBS to a final concentration of

1 mg/ml. For oligomerization, the peptides were further diluted with phenol-free DMEM, then sonicated, incubated at 37°C for 2 hours, followed by incubation at 4°C for 24 hours, and centrifuged at 5000*g* for 50 min before use.

In vitro phagocytosis assay

Microglia and BAMs were isolated, washed, and resuspended in 200 μl of imaging medium containing phenol red–free DMEM supplemented with 10% FBS. These cells were then seeded into μ-slide eight-well chambers (ibidi, Germany) at 10^5 cells per chamber and incubated for 30 min at 5% CO_2 and 37°C. Either pHrodo-conjugated *E. coli* bioparticles (100 μg/ml, Thermo Fisher Scientific, US) or Aβ oligomers (1 μM) were added to each chamber, ensuring even dispersion of the particles. The chambers were incubated at 37°C for 90 min. As a control to evaluate Aβ binding to the cell surface without phagocytic internalization, cells were incubated with Aβ oligomers at 4°C. After two washes, the cells were either collected for flow cytometry analysis or directly observed under a confocal microscope (Zeiss).

In vivo phagocytosis assay

Mice received an intraperitoneal injection of methoxy-XO4 (Abmole, US) at a dosage of 8 mg/kg 3 hours before brain harvesting. Subsequently, the mice were euthanized and perfused with 20 ml of 1× PBS. Cells were isolated, and analysis by flow cytometry included an additional methoxy-XO4 gating step.

Efferocytosis assay

N2A cells were seeded into six-well plates. Upon reaching ~80% confluence, the cells were incubated with 5-chloromethylfluorescein diacetate (CellTracker Green CMFDA dye, Invitrogen, US) diluted in serum-free DMEM to a 1 μM final concentration for 20 min at 37°C, followed by two washes with 1× PBS. Subsequently, cells were cultured with fresh complete medium containing 1 mM H_2O_2 for 20 hours to induce cell apoptosis. One day later, ~10^5 microglia isolated from the mouse brain were seeded in a 24-well plate and left to rest at 37°C for 30 min. The cells were then incubated with CMFDA-labeled apoptotic cells at a ratio of 1:5 (microglia:N2A cells) at 37 or 4°C, respectively, for 2 hours. Microglia were then collected and analyzed by flow cytometry for evidence of CMFDA-labeled N2A cell internalization.

RNA isolation and cDNA preparation

Total RNA was isolated from flow cytometry–sorted cells using the PicoPure RNA Isolation Kit (Thermo Fisher Scientific, US). The Ovation Pico WTA System V2 kit (Tecan, Switzerland) was used to prepare amplified cDNA from the total RNA. All procedures were performed according to the manufacturers' protocols.

Quantitative polymerase chain reaction (qPCR)

All qPCR reactions were run in duplicate with at least three samples in each group. β-Actin was used as the housekeeping gene. The threshold cycle (C_t) values of all the genes were normalized to the C_t value of β-actin. Gene expression fold changes between different groups were calculated using the $2^{-\Delta\Delta Ct}$ method. The following primers were used for qPCR: *Fit2*-forward: CACGACTTGACCCAGAAAGTG; *Fit2*-reverse: GGAGGAAGTCCTGGAGAGAAA; β-actin-forward: AAGGCCAACCGTGAAAAGAT; β-actin-reverse: CCTGTGGTACGACCAGAGGCATACA; *Ccl2*-forward: CACTCACCTGCTGCTACTCA; *Ccl2*-reverse: GCTTGGTGACAAAAACTACAGC; *Ccl4*-forward: ACCCTCCCACTTCCTGCTGTTT; *Ccl4*-reverse: CTGTCTGCCTCTTTTGGTCAGG; *Tnfa*-forward: TGGAGCAACATGTGGAACTC; *Tnfa*-reverse: GTCAGCAGCCGGTTACCA; *Il6*-forward: CTCTGGGAAATCGTGGAAAT; *Il6*-reverse: CCAGTTTGGTAGCATCCATC; *Lpin1*-forward: TAAACGGAGCCGACACCTTGGA; *Lpin1*-reverse: CCGTTGTCACTGGCTTGTTTGG; *Dgat1*-forward: GGTTCCGTGTTTGCTCTGGCAT; *Dgat1*-reverse: CCACTGACCTTCTTCCCTGTAG; *Dgat2*-forward: CTGTGCTCTACTTCACCTGGCT; *Dgat2*-reverse: CTGGATGGGAAAGTAGTCTCGG; *Il1a*-forward: ACGGCTGAGTTTCAGTGAGACC; *Il1a*-reverse: CACTCTGGTAGGTGTAAGGTGC; *Il1b*-forward: GGGCCTCAAAGGAAAGAATC; *Il1b*-reverse: TTCTTCTTTGGGTATTGCTTGG.

Sample preparation for lipidomic analysis

Sorted microglia (2×10^5 cells) obtained from two to three pooled mouse brains were divided into two equal portions. The first half of the cells was treated with precooled methanol (MeOH) containing mixed internal standards of lipids and then with precooled methyl *tert*-butyl ether. After a centrifugation step, the supernatant was desiccated and reconstituted in dichloromethane/MeOH (1:1) for liquid chromatography–mass spectrometry (LC-MS) analysis (C18 and hydrophilic interaction liquid chromatography columns). The second half of the cells was treated with a precooled mixture of water and isopropyl alcohol (IPA) containing mixed internal standards. After a centrifugation step, the supernatant was desiccated and reconstituted in dichloromethane/MeOH (1:1) with 0.1% formic acid for LC-MS analysis (EC C18 column). Quality control samples were prepared by pooling aliquots of all samples. The six quality control samples were analyzed alongside the test samples in each batch to ensure the reliability of the method and the stability of the instrument.

LC-MS analysis

The samples were analyzed on a quadrupole ion-trap-ABSciex QTRAP 6500 (SCIEX, Framingham, MA) mass spectrometer with an electrospray ionization source using the multiple reaction monitoring mode in both positive and negative settings. The instrument was also equipped with a liquid chromatography system (Agilent 1290 Infinity II). The following mass spectrometry parameters were used: The curtain gas value was set at 0.2755 MPa, the collision gas was set to medium, the ionspray voltage was ±4500 V and the source temperature was at 350°C, the pressure for nebulization gas and drying gas were both set to 0.3792 MPa, the entrance potential was ±10 V, and the collision cell exit was 10 V. The methyl *tert*-butyl ether extract was separated using the Phenomenex Kinetex C18 column (2.1 by 100 mm, 2.6 μm) (stream 2) and the Waters BEH HILIC column (2.1 by 100 mm, 1.7 μm) (stream 1) at 45°C. The mobile phase for stream 1 was composed of (A1) water/acetonitrile (5:95, v/v) with 10 mM ammonium acetate and (B1) water/acetonitrile (1:1, v/v) with 10 mM ammonium acetate and 0.01% ammonia-water (28%). The mobile phase for stream 2 was composed of (A2) water/acetonitrile/MeOH (1:1:1, v/v/v) with 7 mM ammonium acetate and (B2) IPA with 7 mM ammonium acetate. The IPA extract was separated using the Agilent Zorbax Eclipse Plus C18 column (2.1 by 100 mm, 1.8 μm) at 50°C with the mobile phase composed of (A) water/acetonitrile/MeOH (1:1:1, v/v/v) with 0.1% formic acid and 1 mM ammonium acetate and (B) IPA/acetonitrile (90:10, v/v) with 0.05% formic acid and 10 mM ammonium acetate. Raw peak areas for the lipid species detected were integrated using SCIEX OS software (version 1.4, AB Sciex Corporation, Framingham, MA) and normalized to the internal standard for each lipid class. All samples were analyzed at random.

Single-cell RNA sequencing (scRNA-seq)

Sorted brain macrophages (90% microglia and 10% BAMs) were processed for scRNA-seq analysis. FASTQ files were obtained for 16 samples, comprising four animals from each of the following four experimental groups: FIT2-WT (6-month-old), FIT2-deficient (6-month-old), APP-KI/FIT2-WT (6-month-old), and APP-KI/FIT2-deficient (6-month-old). All four mouse groups were treated with HFD. 10x Genomics Cell Ranger (version 7.0.0) (*76*) with the chemistry "Single Cell 3' v3" setting was used to align the reads to the GRCm38 mm10-2020-A mouse genome and generate gene counts. Subsequently, the Seurat (version 4.3.0.1) R (version 4.2.1) package was used to analyze gene expression levels (*77*–*79*). Cells with gene counts above the 99th percentile or with unique genes below the first percentile are more likely to be dead cells or doublets, respectively, and were therefore excluded from further analysis (*80*). Cell clusters were identified using a shared nearest-neighbor algorithm via the FindClusters utility (variable genes, 2000; resolution, 0.35; all other parameters as default). The RunUMAP utility (all parameters as default) was used to perform UMAP for cell clustering visualization. Relative gene expression levels between clusters were computed using the FindAllMarkers utility (log.fc threshold = 0; min.pct = 1×10^{-3}; return.threshold = 1; all other parameters as default), which compares the average gene expression in cells inside a cluster to the average gene expression in all cells outside that cluster. The gene expression levels were ranked in reverse Bonferroni-adjusted P value order.

Statistics

Statistical analyses were performed using GraphPad Prism 9.0.1 software. All values were expressed as the means ± standard deviation, unless otherwise stated. Student's t test (two-tailed) was used to determine the significance between the two groups. Comparisons between more than two groups were analyzed by the one-way analysis of variance (ANOVA) or two-way ANOVA. A P value <0.05 was considered as a measure of statistical significance, with the different significance levels denoted as follows: $*P < 0.05$; $**P < 0.01$; $***P < 0.001$; $****P < 0.0001$.

Supplementary Materials

This PDF file includes:
Figs. S1 to S9

REFERENCES AND NOTES

1. J. A. Olzmann, P. Carvalho, Dynamics and functions of lipid droplets. *Nat. Rev. Mol. Cell Biol.* **20**, 137–155 (2019).
2. M. Konige, H. Wang, C. Sztalryd, Role of adipose specific lipid droplet proteins in maintaining whole body energy homeostasis. *Biochim. Biophys. Acta* **1842**, 393–401 (2014).
3. R. C. N. Melo, D. L. Fabrino, F. F. Dias, G. G. Parreira, Lipid bodies: Structural markers of inflammatory macrophages in innate immunity. *Inflamm. Res.* **55**, 342–348 (2006).
4. Y. Gui, H. Zheng, R. Y. Cao, Foam cells in atherosclerosis: Novel insights into its origins, consequences, and molecular mechanisms. *Front. Cardiovasc. Med.* **9**, 845942 (2022).
5. C. Cochain, E. Vafadarnejad, P. Arampatzi, J. Pelisek, H. Winkels, K. Ley, D. Wolf, A. E. Saliba, A. Zernecke, Single-cell RNA-seq reveals the transcriptional landscape and heterogeneity of aortic macrophages in murine atherosclerosis. *Circ. Res.* **122**, 1661–1674 (2018).
6. D. Shim, H. Kim, S. J. Shin, Mycobacterium tuberculosis infection-driven foamy macrophages and their implications in tuberculosis control as targets for host-directed therapy. *Front. Immunol.* **11**, 910 (2020).
7. M. J. Kim, H. C. Wainwright, M. Locketz, L. G. Bekker, G. B. Walther, C. Dittrich, A. Visser, W. Wang, F. F. Hsu, U. Wiehart, L. Tsenova, G. Kaplan, D. G. Russell, Caseation of human tuberculosis granulomas correlates with elevated host lipid metabolism. *EMBO Mol. Med.* **2**, 258–274 (2010).
8. X. Zheng, S. Mansouri, A. Krager, F. Grimminger, W. Seeger, S. S. Pullamsetti, C. E. Wheelock, R. Savai, Metabolism in tumour-associated macrophages: A quid pro quo with the tumour microenvironment. *Eur. Respir. Rev.* **29**, 200134 (2020).
9. G. Marelli, N. Morina, F. Portale, M. Pandini, M. Iovino, G. D. Conza, P.-C. Ho, D. D. Mitri, Lipid-loaded macrophages as new therapeutic target in cancer. *J. Immunother. Cancer* **10**, e004584 (2022).
10. Q. Chen, S. M. Lai, S. Xu, Y. Tan, K. Leong, D. Liu, J. C. Tan, R. R. Naik, A. M. Barron, S. S. Adav, J. Chen, S. Z. Chong, L. G. Ng, C. Ruedl, Resident macrophages restrain pathological adipose tissue remodeling and protect vascular integrity in obese mice. *EMBO Rep.* **22**, e52835 (2021).
11. J. Marschallinger, T. Iram, M. Zardeneta, S. E. Lee, B. Lehallier, M. S. Haney, J. V. Pluvinage, V. Mathur, O. Hahn, D. W. Morgens, J. Kim, J. Tevini, T. K. Felder, H. Wolinski, C. R. Bertozzi, M. C. Bassik, L. Aigner, T. Wyss-Coray, Lipid-droplet-accumulating microglia represent a dysfunctional and proinflammatory state in the aging brain. *Nat. Neurosci.* **23**, 194–208 (2020).
12. D. A. Jaitin, L. Adlung, C. A. Thaiss, A. Weiner, B. Li, H. Descamps, P. Lundgren, C. Bleriot, Z. Liu, A. Deczkowska, H. Keren-Shaul, E. David, N. Zmora, S. M. Eldar, N. Lubezky, O. Shibolet, D. A. Hill, M. A. Lazar, M. Colonna, F. Ginhoux, H. Shapiro, E. Elinav, I. Amit, Lipid-associated macrophages control metabolic homeostasis in a Trem2-dependent manner. *Cell* **178**, 686–698.e14 (2019).
13. M. Arbaizar-Rovirosa, J. Pedragosa, J. J. Lozano, C. Casal, A. Pol, M. Gallizioli, A. M. Planas, Aged lipid-laden microglia display impaired responses to stroke. *EMBO Mol. Med.* **15**, e17175 (2023).
14. H. Keren-Shaul, A. Spinrad, A. Weiner, O. Matcovitch-Natan, R. Dvir-Szternfeld, T. K. Ulland, E. David, K. Baruch, D. Lara-Astaiso, B. Toth, S. Itzkovitz, M. Colonna, M. Schwartz, I. Amit, A unique microglia type associated with restricting development of Alzheimer's disease. *Cell* **169**, 1276–1290.e17 (2017).
15. P. Yuan, C. Condello, C. D. Keene, Y. Wang, T. D. Bird, S. M. Paul, W. Luo, M. Colonna, D. Baddeley, J. Grutzendler, TREM2 haplodeficiency in mice and humans impairs the microglia barrier function leading to decreased amyloid compaction and severe axonal dystrophy. *Neuron* **90**, 724–739 (2016).
16. C. Condello, P. Yuan, A. Schain, J. Grutzendler, Microglia constitute a barrier that prevents neurotoxic protofibrillar Aβ42 hotspots around plaques. *Nat. Commun.* **6**, 6176 (2015).
17. C. Gao, J. Jiang, Y. Tan, S. Chen, Microglia in neurodegenerative diseases: mechanism and potential therapeutic targets. *Signal Transduct. Target Ther.* **8**, 359 (2023).
18. K. I. Mosher, T. Wyss-Coray, Microglial dysfunction in brain aging and Alzheimer's disease. *Biochem. Pharmacol.* **88**, 594–604 (2014).
19. G. Krabbe, A. Halle, V. Matyash, J. L. Rinnenthal, G. D. Eom, U. Bernhardt, K. R. Miller, S. Prokop, H. Kettenmann, F. L. Heppner, Functional impairment of microglia coincides with beta-amyloid deposition in mice with Alzheimer-like pathology. *PLOS ONE* **8**, e60921 (2013).
20. E. G. Njie, E. Boelen, F. R. Stassen, H. W. M. Steinbusch, D. R. Borchelt, W. J. Streit, Ex vivo cultures of microglia from young and aged rodent brain reveal age-related changes in microglial function. *Neurobiol. Aging* **33**, 195.e1–195.e12 (2012).
21. I. Dermitzakis, P. Theotokis, P. Evangelidis, E. Delilampou, N. Evangelidis, A. Chatzisavvidou, E. Avramidou, M. E. Manthou, CNS border-associated macrophages: Ontogeny and potential implication in disease. *Curr. Issues Mol. Biol.* **45**, 4285–4300 (2023).
22. S. Da Mesquita, R. Rua, Brain border-associated macrophages: Common denominators in infection, aging, and Alzheimer's disease? *Trends Immunol.* **45**, 346–357 (2024).
23. A. Drieu, S. Du, S. E. Storck, J. Rustenhoven, Z. Papadopoulos, T. Dykstra, F. Zhong, K. Kim, S. Blackburn, T. Mamuladze, O. Harari, C. M. Karch, R. J. Bateman, R. Perrin, M. Farlow, J. Chhatwal, Dominantly Inherited Alzheimer Network, S. Hu, G. J. Randolph, I. Smirnov, J. Kipnis, Parenchymal border macrophages regulate the flow dynamics of the cerebrospinal fluid. *Nature* **611**, 585–593 (2022).
24. D. A. Miranda, J.-H. Kim, L. N. Nguyen, W. Cheng, B. C. Tan, V. J. Goh, J. S. Y. Tan, J. Yaligar, B. P. Kn, S. S. Velan, H. Wang, D. L. Silver, Fat storage-inducing transmembrane protein 2 is required for normal fat storage in adipose tissue. *J. Biol. Chem.* **289**, 9560–9572 (2014).
25. Z. Yin, D. Raj, N. Saiepour, D. Van Dam, N. Brouwer, I. R. Holtman, B. J. L. Eggen, T. Moller, J. A. Tamm, A. Abdourahman, E. M. Hol, W. Kamphuis, T. A. Bayer, P. P. De Deyn, E. Boddeke, Immune hyperreactivity of Aβ plaque-associated microglia in Alzheimer's disease. *Neurobiol. Aging* **55**, 115–122 (2017).
26. S. Hellwig, A. Masuch, S. Nestel, N. Katzmarski, M. Meyer-Luehmann, K. Biber, Forebrain microglia from wild-type but not adult 5xFAD mice prevent amyloid-β plaque formation in organotypic hippocampal slice cultures. *Sci. Rep.* **5**, 14624 (2015).

27. J. L. Marin-Teva, I. Dusart, C. Colin, A. Gervais, N. van Rooijen, M. Mallat, Microglia promote the death of developing Purkinje cells. *Neuron* **41**, 535–547 (2004).
28. M. Colonna, O. Butovsky, Microglia function in the central nervous system during health and neurodegeneration. *Annu. Rev. Immunol.* **35**, 441–468 (2017).
29. C. Romero-Molina, F. Garretti, S. J. Andrews, E. Marcora, A. M. Goate, Microglial efferocytosis: Diving into the Alzheimer's disease gene pool. *Neuron* **110**, 3513–3533 (2022).
30. J. Miao, H. Ma, Y. Yang, Y. Liao, C. Lin, J. Zheng, M. Yu, J. Lan, Microglia in Alzheimer's disease: Pathogenesis, mechanisms, and therapeutic potentials. *Front. Aging Neurosci.* **15**, 1201982 (2023).
31. H. Van Hove, L. Martens, I. Scheyltjens, K. De Vlaminck, A. R. Pombo Antunes, S. De Prijck, N. Vandamme, S. De Schepper, G. Van Isterdael, C. L. Scott, J. Aerts, G. Berx, G. E. Boeckxstaens, R. E. Vandenbroucke, L. Vereecke, D. Moechars, M. Guilliams, J. A. Van Ginderachter, Y. Saeys, K. Movahedi, A single-cell atlas of mouse brain macrophages reveals unique transcriptional identities shaped by ontogeny and tissue environment. *Nat. Neurosci.* **22**, 1021–1035 (2019).
32. C. Sala Frigerio, L. Wolfs, N. Fattorelli, N. Thrupp, I. Voytyuk, I. Schmidt, R. Mancuso, W.-T. Chen, M. E. Woodbury, G. Srivastava, T. Moller, E. Hudry, S. Das, T. Saido, E. Karran, B. Hyman, V. H. Perry, M. Fiers, B. De Strooper, The major risk factors for Alzheimer's disease: Age, sex, and genes modulate the microglia response to Aβ plaques. *Cell Rep.* **27**, 1293–1306.e6 (2019).
33. L. Cantuti-Castelvetri, D. Fitzner, M. Bosch-Queralt, M. T. Weil, M. Su, P. Sen, T. Ruhwedel, M. Mitkovski, G. Trendelenburg, D. Lutjohann, W. Mobius, M. Simons, Defective cholesterol clearance limits remyelination in the aged central nervous system. *Science* **359**, 684–688 (2018).
34. E. N. Santos, R. D. Fields, Regulation of myelination by microglia. *Sci. Adv.* **7**, eabk1131 (2021).
35. B. A. Loving, K. D. Bruce, Lipid and lipoprotein metabolism in Microglia. *Front. Physiol.* **11**, 393 (2020).
36. R. Y. Li, Q. Qin, H. C. Yang, Y. Y. Wang, Y. X. Mi, Y. S. Yin, M. Wang, C. J. Yu, Y. Tang, TREM2 in the pathogenesis of AD: A lipid metabolism regulator and potential metabolic therapeutic target. *Mol. Neurodegener.* **17**, 40 (2022).
37. T. K. Ulland, M. Colonna, TREM2 — A key player in microglial biology and Alzheimer disease. *Nat. Rev. Neurol.* **14**, 667–675 (2018).
38. C. Claes, E. P. Danhash, J. Hasselmann, J. P. Chadarevian, S. K. Shabestari, W. E. England, T. E. Lim, J. L. S. Hidalgo, R. C. Spitale, H. Davtyan, M. Blurton-Jones, Plaque-associated human microglia accumulate lipid droplets in a chimeric model of Alzheimer's disease. *Mol. Neurodegener.* **16**, 50 (2021).
39. P. Prakash, P. Manchanda, E. Paouri, K. Bisht, K. Sharma, P. R. Wijewardhane, C. E. Randolph, M. G. Clark, J. Fine, E. A. Thayer, A. Crockett, N. Gasmi, S. Stanko, R. A. Prayson, C. Zhang, D. Davalos, G. Chopra, Amyloid β induces lipid droplet-mediated microglial dysfunction in Alzheimer's disease. bioRxiv 543525 [Preprint]. 6 June 2023. https://doi.org/10.1101/2023.06.04.543525.
40. C. L. McDonald, E. Hennessy, A. Rubio-Araiz, B. Keogh, W. McCormack, P. McGuirk, M. Reilly, M. A. Lynch, Inhibiting TLR2 activation attenuates amyloid accumulation and glial activation in a mouse model of Alzheimer's disease. *Brain Behav. Immun.* **58**, 191–200 (2016).
41. C. Hughes, M. L. Choi, J. H. Yi, S. C. Kim, A. Drews, P. S. George-Hyslop, C. Bryant, S. Gandhi, K. Cho, D. Klenerman, Beta amyloid aggregates induce sensitised TLR4 signalling causing long-term potentiation deficit and rat neuronal cell death. *Commun. Biol.* **3**, 79 (2020).
42. L. Zhang, Z. Xie, H. Yu, H. Du, X. Wang, J. Cai, Y. Qiu, R. Chen, X. Jiang, Z. Liu, Y. Li, T. Chen, TLR2 inhibition ameliorates the amplification effect of LPS on lipid accumulation and lipotoxicity in hepatic cells. *Ann. Transl. Med.* **9**, 1429 (2021).
43. C. Lauro, C. Limatola, Metabolic reprograming of microglia in the regulation of the innate inflammatory response. *Front. Immunol.* **11**, 493 (2020).
44. L. H. Fairley, J. H. Wong, A. M. Barron, Mitochondrial regulation of microglial immunometabolism in Alzheimer's disease. *Front. Immunol.* **12**, 624538 (2021).
45. X. Wang, H. Li, Y. Sheng, B. He, Z. Liu, W. Li, S. Yu, J. Wang, Y. Zhang, J. Chen, L. Qin, X. Meng, The function of sphingolipids in different pathogenesis of Alzheimer's disease: A comprehensive review. *Biomed. Pharmacother.* **171**, 116071 (2024).
46. J. Y. Lee, H. K. Jin, J. S. Bae, Sphingolipids in neuroinflammation: A potential target for diagnosis and therapy. *BMB Rep.* **53**, 28–34 (2020).
47. F. Taheri, E. Taghizadeh, J. G. Navashenaq, M. Rezaee, S. M. Gheibihayat, The role of efferocytosis in neuro-degenerative diseases. *Neurol. Sci.* **43**, 1593–1603 (2022).
48. K. Liu, M. J. Czaja, Regulation of lipid stores and metabolism by lipophagy. *Cell Death Differ.* **20**, 3–11 (2013).
49. F. Cabrera-Reyes, C. Parra-Ruiz, M. I. Yuseff, S. Zanlungo, Alterations in lysosome homeostasis in lipid-related disorders: Impact on metabolic tissues and immune cells. *Front. Cell Dev. Biol.* **9**, 790568 (2021).
50. T. Fernandes, M. R. Domingues, P. I. Moreira, C. F. Pereira, A perspective on the link between Mitochondria-Associated Membranes (MAMs) and lipid droplets metabolism in neurodegenerative diseases. *Biology* **12**, 414 (2023).
51. L. H. Fairley, K. O. Lai, J. H. Wong, W. J. Chong, A. S. Vincent, G. D'Agostino, X. Wu, R. R. Naik, A. Jayaraman, S. R. Langley, C. Ruedl, A. M. Barron, Mitochondrial control of microglial phagocytosis by the translocator protein and hexokinase 2 in Alzheimer's disease. *Proc. Natl. Acad. Sci. U.S.A.* **120**, e2209177120 (2023).
52. S. Jativa, P. Calle, S. Torrico, A. Munoz, M. Garcia, I. Martinez, A. Sola, G. Hotter, Mitochondrial transplantation enhances phagocytic function and decreases lipid accumulation in foam cell macrophages. *Biomedicine* **10**, 329 (2022).
53. M. P. Tobin, I. L. Ivanovska, D. E. Discher, Small fat droplets interact with structural filaments in macrophages with cytoskeletal dysfunction contributing to perturbed phagocytosis and migration. *Biophys. J.* **122**, 409a (2023).
54. Y. Yoo, G. Neumayer, Y. Shibuya, M. M.-D. Mader, M. Wernig, A cell therapy approach to restore microglial Trem2 function in a mouse model of Alzheimer's disease. *Cell Stem Cell* **30**, 1043–1053.e6 (2023).
55. K. Biber, Reestablishing microglia function: Good news for Alzheimer's therapy? *EMBO J.* **36**, 565–567 (2017).
56. M. R. P. Elmore, L. A. Hohsfield, E. A. Kramar, L. Soreq, R. J. Lee, S. T. Pham, A. R. Najafi, E. E. Spangenberg, M. A. Wood, B. L. West, K. N. Green, Replacement of microglia in the aged brain reverses cognitive, synaptic, and neuronal deficits in mice. *Aging Cell* **17**, e12832 (2018).
57. T. C. Walther, J. Chung, R. V. Farese Jr., Lipid droplet biogenesis. *Annu. Rev. Cell Dev. Biol.* **33**, 491–510 (2017).
58. B. Kadereit, P. Kumar, W. J. Wang, D. Miranda, E. L. Snapp, N. Severina, I. Torregroza, T. Evans, D. L. Silver, Evolutionarily conserved gene family important for fat storage. *Proc. Natl. Acad. Sci. U.S.A.* **105**, 94–99 (2008).
59. X. Zheng, Q. W. C. Ho, M. Chua, O. Stelmashenko, X. Y. Yeo, S. Muralidharan, F. Torta, E. G. Y. Chew, M. M. Lian, J. N. Foo, S. Jung, S. H. Wong, N. S. Tan, N. Tong, G. A. Rutter, M. R. Wenk, D. L. Silver, P.-O. Berggren, Y. Ali, Destabilization of β Cell FIT2 by saturated fatty acids alter lipid droplet numbers and contribute to ER stress and diabetes. *Proc. Natl. Acad. Sci. U.S.A.* **119**, e2113074119 (2022).
60. K. Mittal, E. Eremenko, O. Berner, Y. Elyahu, I. Strominger, D. Apelblat, A. Nemirovsky, I. Spiegel, A. Monsonego, CD4 T cells induce a subset of MHCII-expressing microglia that attenuates Alzheimer pathology. *iScience* **16**, 298–311 (2019).
61. A. Grubman, X. Y. Choo, G. Chew, J. F. Ouyang, G. Sun, N. P. Croft, F. J. Rossello, R. Simmons, S. Buckberry, D. V. Landin, J. Pflueger, T. H. Vandekolk, Z. Abay, Y. Zhou, X. Liu, J. Chen, M. Larcombe, J. M. Haynes, C. McLean, S. Williams, S. Y. Chai, T. Wilson, R. Lister, C. W. Pouton, A. W. Purcell, O. J. L. Rackham, E. Petretto, J. M. Polo, Transcriptional signature in microglia associated with Aβ plaque phagocytosis. *Nat. Commun.* **12**, 3015 (2021).
62. Q. Luo, N. Zheng, L. Jiang, T. Wang, P. Zhang, Y. Liu, P. Zheng, W. Wang, G. Xie, L. Chen, D. Li, P. Dong, X. Yuan, L. Shen, Lipid accumulation in macrophages confers protumorigenic polarization and immunity in gastric cancer. *Cancer Sci.* **111**, 4000–4011 (2020).
63. W. Wei, L. Zhang, W. Xin, Y. Pan, L. Tatenhorst, Z. Hao, S. T. Gerner, S. Huber, M. Juenemann, M. Butz, H. B. Huttner, M. Bahr, D. Fitzner, F. Jia, T. R. Doeppner, TREM2 regulates microglial lipid droplet formation and represses post-ischemic brain injury. *Biomed. Pharmacother.* **170**, 115962 (2024).
64. H. Li, P. Liu, S. Deng, L. Zhu, X. Cao, X. Bao, S. Xia, Y. Xu, B. Zhang, Pharmacological upregulation of microglial lipid droplet alleviates neuroinflammation and acute ischemic brain injury. *Inflammation* **46**, 1832–1848 (2023).
65. S. De Schepper, J. Z. Ge, G. Crowley, L. S. S. Ferreira, D. Garceau, C. E. Toomey, D. Sokolova, J. Rueda-Carrasco, S. H. Shin, J. S. Kim, T. Childs, T. Lashley, J. J. Burden, M. Sasner, C. Sala Frigerio, S. Jung, S. Hong, Perivascular cells induce microglial phagocytic states and synaptic engulfment via SPP1 in mouse models of Alzheimer's disease. *Nat. Neurosci.* **26**, 406–415 (2023).
66. J. Rustenhoven, A. Drieu, T. Mamuladze, K. A. de Lima, T. Dykstra, M. Wall, Z. Papadopoulos, M. Kanamori, A. F. Salvador, W. Baker, M. Lemieux, S. D. Mesquita, A. Cugurra, J. Fitzpatrick, S. Sviben, R. Kossina, P. Bayguinov, R. R. Townsend, Q. Zhang, P. Erdmann-Gilmore, I. Smirnov, M.-B. Lopes, J. Herz, J. Kipnis, Functional characterization of the dural sinuses as a neuroimmune interface. *Cell* **184**, 1000–1016.e27 (2021).
67. G. Faraco, Y. Sugiyama, D. Lane, L. Garcia-Bonilla, H. Chang, M. M. Santisteban, G. Racchumi, M. Murphy, N. Van Rooijen, J. Anrather, C. Iadecola, Perivascular macrophages mediate the neurovascular and cognitive dysfunction associated with hypertension. *J. Clin. Invest.* **126**, 4674–4689 (2016).
68. C. A. Hawkes, J. McLaurin, Selective targeting of perivascular macrophages for clearance of β-amyloid in cerebral amyloid angiopathy. *Proc. Natl. Acad. Sci. U.S.A.* **106**, 1261–1266 (2009).
69. K. Uekawa, Y. Hattori, S. J. Ahn, J. Seo, N. Casey, A. Anfray, P. Zhou, W. Luo, J. Anrather, L. Park, C. Iadecola, Border-associated macrophages promote cerebral amyloid angiopathy and cognitive impairment through vascular oxidative stress. *Mol. Neurodegener.* **18**, 73 (2023).
70. A. Latif-Hernandez, D. Shah, K. Craessaerts, T. Saido, T. Saito, B. De Strooper, A. Van der Linden, R. D'Hooge, Subtle behavioral changes and increased prefrontal-

hippocampal network synchronicity in APP^{NL-G-F} mice before prominent plaque deposition. *Behav. Brain Res.* **364**, 431–441 (2019).

71. J.-Z. Wang, Y.-Y. Xia, I. Grundke-Iqbal, K. Iqbal, Abnormal hyperphosphorylation of tau: sites, regulation, and molecular mechanism of neurofibrillary degeneration. *J. Alzheimers Dis.* **33**, S123–S139 (2013).
72. P. Rawat, U. Sehar, J. Bisht, A. Selman, J. Culberson, P. H. Reddy, Phosphorylated Tau in Alzheimer's disease and other tauopathies. *Int. J. Mol. Sci.* **23**, 12841 (2022).
73. M. Wang, G. Tang, C. Zhou, H. Guo, Z. Hu, Q. Hu, G. Li, Revisiting the intersection of microglial activation and neuroinflammation in Alzheimer's disease from the perspective of ferroptosis. *Chem. Biol. Interact.* **375**, 110387 (2023).
74. T. Saito, Y. Matsuba, N. Mihira, J. Takano, P. Nilsson, S. Itohara, N. Iwata, T. C. Saido, Single App knock-in mouse models of Alzheimer's disease. *Nat. Neurosci.* **17**, 661–663 (2014).
75. X. Wu, T. Saito, T. C. Saido, A. M. Barron, C. Ruedl, Microglia and CD206$^+$ border-associated mouse macrophages maintain their embryonic origin during Alzheimer's disease. *eLife* **10**, e71879 (2021).
76. G. X. Y. Zheng, J. M. Terry, P. Belgrader, P. Ryvkin, Z. W. Bent, R. Wilson, S. B. Ziraldo, T. D. Wheeler, G. P. McDermott, J. Zhu, M. T. Gregory, J. Shuga, L. Montesclaros, J. G. Underwood, D. A. Masquelier, S. Y. Nishimura, M. Schnall-Levin, P. W. Wyatt, C. M. Hindson, R. Bharadwaj, A. Wong, K. D. Ness, L. W. Beppu, H. J. Deeg, C. McFarland, K. R. Loeb, W. J. Valente, N. G. Ericson, E. A. Stevens, J. P. Radich, T. S. Mikkelsen, B. J. Hindson, J. H. Bielas, Massively parallel digital transcriptional profiling of single cells. *Nat. Commun.* **8**, 14049 (2017).
77. Z. A. Xia, Y. Zhou, J. Li, J. He, Integrated analysis of single-cell and bulk RNA-sequencing reveals a tissue-resident macrophage-related signature for predicting immunotherapy response in breast cancer patients. *Cancers* **14**, 5506 (2022).
78. T. Stuart, A. Butler, P. Hoffman, C. Hafemeister, E. Papalexi, W. M. Mauck III, Y. Hao, M. Stoeckius, P. Smibert, R. Satija, Comprehensive integration of single-cell data. *Cell* **177**, 1888–1902.e21 (2019).
79. A. Butler, P. Hoffman, P. Smibert, E. Papalexi, R. Satija, Integrating single-cell transcriptomic data across different conditions, technologies, and species. *Nat. Biotechnol.* **36**, 411–420 (2018).
80. A. S. Bais, D. Kostka, scds: Computational annotation of doublets in single-cell RNA sequencing data. *Bioinformatics* **36**, 1150–1158 (2020).

Acknowledgments: We would like to thank E. Lee for mouse management, L. Xu for conducting lipidomic analysis, Singapore Phenome Centre for providing the platform for lipidomic analysis, A. M. Barron and J. H. Wong for providing the N2A cell line and guidance on Aβ oligomerization, and Insight Editing London for proofreading the manuscript before submission. **Funding:** This work was supported by the Ministry of Education Tier2 grant **(**MOE-T2EP30121-0004**)** awarded to C.R. **Author contributions:** Methodology: X.W., C.R., and B.T.K.L. Writing—original draft: X.W. and C.R. Writing—review and editing: X.W., C.R., and B.T.K.L. Data curation: X.W., J.A.M., B.T.K.L., and C.R. Formal analysis: X.W., J.A.M., B.T.K.L., Y.W., and C.R. Software: J.A.M. Visualization: X.W., J.A.M., B.T.K.L., Y.W., and C.R. Investigation: X.W. and Y.W. Resources: X.W., B.T.K.L., and C.R. Validation: X.W., B.T.K.L., and C.R. Project administration: X.W., B.T.K.L., and C.R. Conceptualization: C.R. and X.W. Supervision: B.T.K.L. and C.R. Funding acquisition: C.R. **Competing interests:** The authors declare that they have no competing interests. **Data and materials availability:** scRNA-seq data have been deposited into the NCBI GEO repository as GSE267137. Original lipidomic data (Excel file) and flow cytometry FlowJo data are deposited in the NTU Open Access Data Repository DR-NTU (https://doi.org/10.21979/N9/V4FHSQ). All data needed to evaluate the conclusions in the paper are present in the paper and/or the Supplementary Materials.

Submitted 22 May 2024
Accepted 3 January 2025
Published 5 February 2025
10.1126/sciadv.adq6038